The Analyser of Space Plasmas and Energetic Atoms (ASPERA-4) for the Venus Express mission

S. Barabash[a,*], J.-A. Sauvaud[b], H. Gunell[a], H. Andersson[a], A. Grigoriev[a], K. Brinkfeldt[a], M. Holmström[a], R. Lundin[a], M. Yamauchi[a], K. Asamura[c], W. Baumjohann[d], T.L. Zhang[d], A.J. Coates[e], D.R. Linder[e], D.O. Kataria[e], C.C. Curtis[f], K.C. Hsieh[f], B.R. Sandel[f], A. Fedorov[b], C. Mazelle[b], J.-J. Thocaven[b], M. Grande[g], Hannu E.J. Koskinen[h,i], E. Kallio[i], T. Säles[i], P. Riihela[i], J. Kozyra[j], N. Krupp[k], J. Woch[k], J. Luhmann[l], S. McKenna-Lawlor[m], S. Orsini[n], R. Cerulli-Irelli[n], M. Mura[n], M. Milillo[n], M. Maggi[n], E. Roelof[o], P. Brandt[o], C.T. Russell[p], K. Szego[q], J.D. Winningham[r], R.A. Frahm[r], J. Scherrer[r], J.R. Sharber[r], P. Wurz[s], P. Bochsler[s]

[a]Swedish Institute of Space Physics, Box 812, SE-981 28 Kiruna, Sweden
[b]Centre d'Etude Spatiale des Rayonnements, BP-4346, F-31028 Toulouse, France
[c]Institute of Space and Astronautical Science, 3-1-1 Yoshinodai, Sagamichara, Japan
[d]Space Research Institute, Austrian Academy of Sciences, Schmiedstrasse 6, 8042, Graz, Austria
[e]Mullard Space Science Laboratory, University College London, Surrey RH5 6NT, UK
[f]University of Arizona, Tucson, AZ 85721, USA
[g]University of Wales, Aberystwyth Penglais, Aberystwyth, Ceredigion, SY23 3BZ, UK
[h]Department of Physical Sciences, University of Helsinki, P.O. Box 64, 00014 Helsinki, Finland
[i]Finnish Meteorological Institute, Box 503, FIN-00101 Helsinki, Finland
[j]Space Physics Research Laboratory, University of Michigan, Ann Arbor, MI 48109-2143, USA
[k]Max Planck Institut für Sonnensystemforschung, D-37191 Katlenburg-Lindau, Germany
[l]Space Science Laboratory, University of California at Berkeley, Berkeley, CA 94720-7450, USA
[m]Space Technology Ireland., National University of Ireland, Maynooth, Co. Kildare, Ireland
[n]Instituto di Fisica dello Spazio Interplanetari, I-00133 Rome, Italy
[o]Applied Physics Laboratory, Johns Hopkins University, Laurel, MD 20723-6099, USA
[p]Institute of Geophysics and Planetary Physics, University of California, Los Angeles, CA 90024-1567, USA
[q]KFKI Research Institute for Particle and Nuclear Physics, Konkoly Thege Miklós út 29-33, H-1121 Budapest, Hungary
[r]Southwest Research Institute, San Antonio, TX 7228-0510, USA
[s]University of Bern, Physikalisches Institut, CH-3012 Bern, Switzerland

Abstract

The general scientific objective of the ASPERA-4 (Analyser of Space Plasmas and Energetic Atoms) experiment is to study the solar wind–atmosphere interaction and characterise the plasma and neutral gas environment in the near-Venus space through energetic neutral atom (ENA) imaging and local charged particle measurements. The studies to be performed address the fundamental question: How strongly do the interplanetary plasma and electromagnetic fields affect the Venusian atmosphere? The ASPERA-4 instrument comprises four sensors; two ENA sensors, electron and ion spectrometers. The neutral particle imager (NPI) provides measurements of the integral ENA flux (0.1–60 keV) with no mass and energy resolution but relatively high angular resolution. The neutral particle detector (NPD) provides measurements of the ENA flux, resolving velocity (0.1–10 keV) and mass (H and O) with a coarse angular resolution. The electron spectrometer (ELS) is a standard top-hat electrostatic analyser in a very compact design. These three sensors are located on a

*Corresponding author.
E-mail address: stas.barabash@irf.se (S. Barabash).

scanning platform providing a 4π coverage. The instrument also contains an ion mass composition sensor, IMA (ion mass analyser). Mechanically, IMA is a separate unit electrically connected with the ASPERA-4 main unit. IMA provides ion measurements in the energy range 0.01–36 keV/q for the main ion components H^+, He^{++}, He^+, and the ion group with M/q 20–80 amu/q.

1. The science

1.1. Scientific objectives for plasma measurements at Venus

Venus, Earth and Mars, the three largest terrestrial planets, have undergone much different thermal and atmospheric evolution. Mars has evolved rapidly. Initially, we now believe, Mars had a strong internally driven magnetic shield over an atmosphere much denser than present, one possibly supporting rain and flowing water on the surface. But the interior cooled rapidly, the dynamo stopped and much of the atmosphere escaped (Acuña et al., 1998; Schubert et al., 2000). Earth in contrast still has its magnetic field, a substantial atmosphere and abundant water. Venus may be the least evolved of the three planets. A thick crust has kept the interior hot but at the same time stifled the heat flow needed to drive convection in the fluid iron core. Thus Venus has no magnetic shield against the solar wind and perhaps never had (Russell et al., 1980). Venus has a very dense atmosphere but very little water. Clearly the Venus atmosphere has evolved greatly since the planet accreted, yet still much atmosphere remains. Possibly the escape mechanism is very selective favouring the escape of water, or perhaps hydrogen, leaving the oxygen to combine with the soil. We do not know because no mission to Venus was instrumented to address this objective. Therefore, the main scientific objective of the ASPERA-4 (Analyser of Space Plasmas and Energetic Atoms) experiment is to study solar wind induced atmospheric escape. The specific scientific questions to be addressed are:

- How is the Venus atmosphere coupled with the solar wind? How is mass added to and removed from the atmosphere due to this coupling?
- What is the structure of the interaction region?
- The previous question is connected to the issue of "where did the water go?" The early atmosphere must have contained water equivalent to a few meters deep global ocean as follows from the H/D ratio consideration (Donahue and Hartle, 1992). Could the solar wind interaction have contributed to the water escape (mainly increasing H escape)? Is the process the same as for the water escape from Mars?
- What is the mass composition of the escaping plasma? To what degree are the outflow processes mass dependent, and can this explain the Venus loss of water and greenhouse effect?

- What is the neutral–plasma interaction on Venus? How does the presence of the neutral gas affect plasma dynamics?
- What are similarities and differences in the solar wind interaction with the other terrestrial planets, Earth and Mars?

None of the previous missions to Venus covered such a wide range of scientific objectives. The other uniqueness of the instrument is that ASPERA-4 is a replica of the ASPERA-3 experiment orbiting Mars on board the ESA Mars Express mission (Barabash et al., 2007). The combination of the observations made by two identical instruments at two non-magnetised planets exhibiting the similar type of the solar wind interaction but differing significantly in terms of interplanetary conditions, atmospheric characteristics, and size and mass opens completely a new perspective for comparative magnetospheric studies.

1.2. Required measurements

In order to study the escape of the present day Venus atmosphere one must measure the incident solar wind flux, and the escaping ions whose thermal and bulk velocities will range from about 10–1000 km s^{-1}, depending on the mechanism at work. Since O_2^+ ions dissociatively recombine forming a hot oxygen corona out to 4000 km altitude, oxygen ions will be picked up in the solar wind as well as accelerated down the wake or tail of Venus on the night side. Charge exchange between the solar wind and the neutral Venus atmosphere should be an important process because of the Venus dense upper atmosphere. Thus energetic neutral atoms (ENA) (Gunell et al., 2005b) and, possibly X-rays (Holmström et al., 2001), will be generated. This opens up the possibility to image the interaction region in order to obtain instantaneous images of the global distribution of the solar wind and planetary plasmas and qualify the instantaneous escape induced by the solar wind. These measurements should be designed to detect both hydrogen and oxygen atoms at velocities near 400 km s^{-1}. The current estimates of the ion loss rate are around 10^{24} ions/s (Moore et al., 1991). Ion and ENA measurements should be supported by the electron measurements to characterise the local plasma conditions and identify the main plasma domains. Therefore, the ASPERA-4 experiment includes four sensors: the electron spectrometer (ELS); the ion mass analyser (IMA); the

neutral particle imager (NPI); and the neutral particle detector (NPD).

In order to characterise the environment of the picked up ions and understand the mechanism involved in their acceleration the magnetic field must be measured. The ambient magnetic field encountered will range from about 1 to 200 nT and typically range from 10 to 30 nT. Since some spacecraft magnetic field will be present, a range of up to 1000 nT is recommended with gradiometer sensors along a modest (0.5 m) boom with monitoring of current levels of critical sources of stray magnetic fields. The magnetometer MAG (Venus Express Magnetometer) is included in the Venus Express payload (Zhang and et al., 2006).

1.3. The solar wind–atmosphere interaction

Near-Venus space is strikingly different from Earth-space because of the absence of a intrinsic magnetic field of Venus. Without the magnetic cavity of a magnetosphere to shield the upper atmosphere from the on-coming solar wind, Venus is subject to comet-like atmosphere erosion processes and solar-wind-induced current systems that have no terrestrial counterparts. From experience gained in orbit around Venus on the Pioneer Venus Orbiter (PVO), we have developed ideas of how the upper atmosphere and solar wind interact and the consequences for the planet. In particular, we have observed that the scavenging of planetary ions removes heavy constituents such as oxygen, which plays an important role in the atmosphere's hydration and surface oxidation history.

The current atmospheric conditions on Venus indicate that water is present in only trace amounts ($\sim$ a few precipitable micrometers), much less than expected if Venus' early atmosphere was Earth-like. In contrast to the Martian water story (McKay and Stoker, 1989) it is unlikely to be frozen and buried or sequestered in polar ice caps. Thus the alternative of escape to space in the form of water's constituents is most likely. It is relatively easy to lose light hydrogen, but oxygen loss is problematic. Small amounts can escape via the production of a hot atomic oxygen corona from ionospheric photochemistry (Nagy et al., 1981), but the bulk of the O_2 and O are gravitationally bound. Independent analyses of surface oxidation on the planet indicates that most of the oxygen left over from photo-dissociation over the history of Venus did not become incorporated into the exposed rocks and soil. What could produce such an effective oxygen escape mechanism? Could the processes associated with the solar wind interaction account for the escape of sufficient quantities of oxygen to have made an Earth-like water budget for Venus $\sim$4 Gyr ago?

ASPERA-4 includes four sensors: NPI, NPD, IMA, and ELS each of which contributes, both alone and in combination, to understanding the different consequences of direct solar wind interaction with a planetary atmosphere/ionosphere. Because Venus does not have the complication of the Martian remanent magnetic fields, and has the initial comprehensive reconnaissance provided by PVO (Pioneer Venus Orbiter), the ASPERA-4 measurements that fill in the knowledge gaps left by PVO will make progress in our understanding far exceeding its own coverage of the Venus solar wind interaction physics. In particular, the IMA puts a definitive composition label on the atmospheric pickup ions produced at Venus and detect them over a much greater (up to 36 keV as opposed to PVO's $\sim$8 keV) energy range. The ELS measures both low energy escaping plasma and high energy electrons that contribute to the ion production through electron impact ionisation. The ENAs detected by NPD and NPI provides a measure of solar wind energy deposited in the atmosphere that cannot be estimated from the plasma and field measurements alone, as described below.

A combination of PVO results led to our current picture of atmospheric oxygen escape from Venus. The UV spectrometer (Stewart, 1980) confirmed the existence of an atomic oxygen upper atmosphere extending well into the magnetosheath. This hot O "corona" was shown by Nagy et al. (1981) to agree with models of photochemical exospheres produced by dissociative recombination in the O_2^+ ionosphere. Combined magnetometer (Russell et al., 1980) and plasma analyser (Mihalov et al., 1980; Intriligator et al., 1980) measurements were then used to construct a scenario of both direct O^+ pickup ion escape (Moore et al., 1990) and additional sputtering of O from the atmosphere by impacting O^+ pickup ions not on direct escape trajectories (Luhmann and Kozyra, 1991). The pickup ions can be created by any ionisation mechanism—photoionisation, solar wind electron impact, or charge exchange with solar wind protons, in all atmospheric regions above the exobase ($\sim$200 km altitude) penetrated by the solar wind convection electric field. There are also suggestions of other possible ion removal processes in the thermal plasma (below a few eV) energy range at work at the ionopause boundary layer (Brace et al., 1982) and in the low altitude wake (Hartle and Grebowsky, 1990), distinct from the pickup ion-related mechanisms, which we do not discuss here. In any case, the limited capabilities of the PVO instruments for measuring both solar wind electrons and magnetosheath protons (where the upper atmosphere penetration occurs), as well as solid identification of the pickup ions composition, made it difficult to quantify the details of the escape scenario. The ASPERA-4 IMA, with the added magnetometer MAG, on Venus Express should finally allow the evaluation of escape rates for oxygen ions as well as other species, their variation with interplanetary conditions, and their implications for related sputtering losses.

Another problem of the solar wind—atmosphere coupling that has not been explored experimentally concerns the energetic consequences for the Venusian atmosphere of the lack of a planetary dipole field of any importance. Kinetic and test-particle models of the Mars–solar wind interaction (Brecht, 1997; Kallio et al., 1997) suggest that

solar wind absorption by the Martian atmosphere may be an important energy source for the upper atmosphere at that planet. However, at Venus the much smaller relative solar wind proton gyroradii greatly limit the numbers of protons that can reach the exobase which is well below the ionopause ($\sim$200 km exobase altitude compared to $\sim$300 km ionopause altitude. A solar wind proton gyroradius in the inner magnetosheath is typically $\sim$10 km). ENA production in the magnetosheath by charge exchange between solar wind protons and the exosphere/thermosphere near the solar wind/ionosphere boundary decouples the energetic neutralised protons from the magnetic field in the sheath, leaving them free to impact the exobase (e.g. Kallio et al., 1997). The ENAs generated as a product of the solar wind interaction can thus greatly enhance the deposition of solar wind energy into the upper atmosphere (Kallio and Barabash, 2000) and, at the same time, provide a means of "imaging" the solar wind interaction. Fok et al. (2004) and Gunell et al. (2005b) have modelled the ENA production at Venus using MHD simulations. The NPD will provide tests of the predicted fluxes and composition of the ENAs, while imaging these particles with NPI will show the spots or regions of the most intense ENA precipitation, and give information on their variation with solar wind conditions.

While the energy transfer associated with the ENA precipitation can be important, for the thermal structure of the upper atmosphere, it is the O^+ pickup ion precipitation that causes significant sputtering-induced loss of the atmosphere. Luhmann and Kozyra (1991) estimated that O^+ sputtering results in the escape of oxygen atoms from Venus at rates comparable to sputtering losses from the much smaller planet Mars (Luhmann and Bauer, 1992). Comparisons of ASPERA-3 results from Mars Express with ASPERA-4 results will provide an invaluable look at the processes and rates by which unmagnetised terrestrial planet atmospheres evolve due to their solar wind interactions.

1.4. Pickup ions at Venus

Observations of oxygen pickup ions by the plasma analyser on PVO sparked broad interest in solar wind erosion of unmagnetised planet atmospheres with its first-order picture of the spatial distribution and energies of O^+ pickup ions. These results, collected during PVO's $\sim$14 year, $\sim$5000 orbit tour, provide an idea of what is to be expected from IMA measurements on Venus Express.

The PVO plasma analyser (PV OPA) has been described in the literature a number of times (Intriligator et al., 1980; Mihalov and Barnes, 1982; Moore et al., 1990). Its key features included its $\sim$8 keV/q energy per charge upper limit for detection and a directional sampling scheme, providing approximately 15° azimuthal and 20$-$30° polar angle resolution with respect to the PVO spin axis. The time resolution for a full angle and energy scan was about 9 min, which gave only a few samples during each periapsis

pass. Thus the best observations of pickup ions were generally obtained during apoapsis at about 12 planetary radii downstream. The energy and angular coverage limitation implies that a significant amount of the O^+ present was not detected on PVO.

The energies and orbital locations of the oxygen peaks differ from orbit to orbit due to the variability of the solar wind and especially the cross-flow interplanetary magnetic field orientation. The cross-flow interplanetary field orientation creates changing asymmetries in the O^+ spatial distribution due to the large gyroradii of O^+ ions ($\sim$0.5$-$1.0R_v, R_v is the Venus Radius) relative to the size of the planet and the solar wind interaction region. Because the direction of the interplanetary magnetic field is usually eastward or westward, the convection electric field $\vec{E} = -\vec{v} \times \vec{B}$ (where $\vec{v}$ is the solar wind plasma velocity and $\vec{B}$ the local magnetic field) produces pickup ion trajectories that are initially either northward or southward as well as antisunward. If the ion trajectory does not intersect the exobase at a few hundred kilometres altitude, the trajectory continues down the wake, forming a one-sided ion stream. Thus near the planet terminator and in the near-planet wake, one typically observes O^+ detection locations organised into northern or southern spatial clusters (Moore et al., 1990; Intriligator et al., 1979).

The PVO results suggest the extent to which ASPERA-4 on Venus Express with its energy range of 10 eV to 36 keV, scanning field of view, and ability to separate ion masses, will greatly improve our view of the pickup ion environment around Venus. The currently planned Venus Express orbit is similar to that of PVO, but with periapsis at $\sim$65°N Latitude and a periapsis of 250–400 km, compared to PVO's 15°N Latitude initial periapsis and nominal $\sim$160 km periapsis. The Venus Express orbit thus provides a somewhat different perspective, focusing on the magnetosheath, near-terminator, and low altitude wake pickup ion characteristics rather than on the distant pickup ion wake characteristics. This is in fact highly complementary to the PVO orbit geometry sampling which did not allow coverage of the low altitude wake. If the orbit is allowed to evolve so that the sampling region circularises, a broader sampling will be obtained.

1.5. ENA production at Venus

ENAs are produced in charge exchange collisions between solar wind protons and neutral atoms in the upper part of the atmospheres of the planets. The ASPERA-4 instrument provides ENA images of the Venus–solar wind interaction region. Such images have been simulated through the integration of the ENA production along lines of sight to a virtual ENA instrument (Fok et al., 2004; Gunell et al., 2005b). Some of the results from these simulation studies are reviewed here.

Venus Express arrives at Venus during solar minimum conditions. Due to the scarcity of in situ measurements the ionopause altitude at Venus is not well known for solar

minimum conditions (Luhmann, 1992). It is thought to vary with the solar cycle, but since all in situ measurements were made during solar maximum conditions this variation is still unconfirmed. Gunell et al. (2005b) have investigated the ENA emissions as a function of ionopause distance by scaling the ionopause altitude in the plasma model. The ENA flux from the local emission maximum near the planet decreases with increasing ionopause altitude, since with a higher ionopause altitude the protons pass through a region with lower neutral density. This also affects the ENA production and escape rates. The ionopause is thought to be close to the lower end of that range at solar minimum because of the lower ionospheric pressure (Luhmann, 1992). The ENA images are then generated by evaluating line of sight integrals in the same way as it has previously been done to simulate ENA images of the Martian environment (Holmström et al., 2002; Gunell et al., 2005a). Gunell et al. (2005b) have used a semi-analytical MHD model (Biernat et al., 1999, 2000, 2001) to describe the plasma flow around Venus, and a neutral gas density model that is based on published data from measurements.

The maximum flux observed at $3R_v$ planetocentric distance, coming from the interaction region on the dayside of Venus is $5.8 \times 10^{10} \, \text{sr}^{-1} \, \text{m}^{-2} \, \text{s}^{-1}$, which occurs for the lowest ionopause altitude, i.e., 250 km. The ENAs that are produced in the solar wind upstream of the bow shock are not included in this number. For higher ionopause altitudes the ENA flux decreases, and is below $3.8 \times 10^{10} \, \text{sr}^{-1} \, \text{m}^{-2} \, \text{s}^{-1}$, when the subsolar ionopause is at 400 km altitude. The corresponding number for Mars at solar minimum conditions, computed by Holmström et al. (2002) is about $3 \times 10^{11} \, \text{sr}^{-1} \, \text{m}^{-2} \, \text{s}^{-1}$, which is five times larger than the value obtained for Venus with an ionopause altitude of 250 km. The ENA production rate at Mars at solar maximum conditions is about the same as that at Venus.

The ENA flux and production rates at Venus are lower than at Mars even though the solar wind flux is greater at Venus. The reason for this is that the neutral gas density at relevant heights is lower in Venus' than Mars' exosphere. The neutral density falls off more rapidly with altitude at Venus, because of the larger mass of that planet, which is 7.5 times greater than the mass of Mars. The dominant contribution to the neutral density at high altitudes at Mars during solar minimum conditions is the large hydrogen corona (Krasnopolsky and Gladstone, 1996). The hydrogen density at Mars is greater than that at Venus everywhere above the exobase, and hydrogen is by far the most important species for ENA production at Mars (Holmström et al., 2002).

It is interesting to compare the results obtained by Gunell et al. (2005b) with the results of Fok et al. (2004). Although the parameters used in the two papers are not exactly the same they are at least similar. Fok et al. (2004) took the effect of spacecraft motion into account. Since Gunell et al. (2005b) are considering ENAs with energies above 50 eV this amounts only to a small correction in their case. Both models yield ENA fluxes of the same order of magnitude, and one can conclude that the two models are in reasonable agreement considering the uncertainties of the models. Real measurements will be required to determine between them, or indeed to say anything conclusively about the accuracy of the models.

2. The instrument

2.1. Overall configuration

The ASPERA-4 instrument is a replica of ASPERA-3 on board Mars Express mission (Barabash et al., 2007). The experiment is a comprehensive plasma diagnostic package to measure ENAs, electrons, and ions with a wide angular coverage from a three axis stabilised platform. Mechanically, ASPERA-4 consists of two units, the main unit (MU) and the IMA (Fig. 1). The MU comprises three sensors: the neutral particle imager (NPI), the neutral particle detector (NPD), the electron spectrometer (ELS), and a digital processing unit (DPU), which all are located on a turnable platform. The combination of the 360° sensor field of view (180° for the NPD) and the scans from 0° to 180° give, ideally, the required 4π maximum coverage, but part of the field of view is blocked by the spacecraft body. The real coverage depends on the instrument location on the spacecraft. All electrical interfaces of the instrument with the spacecraft are made through the scanner. Electrically IMA interfaces only MU. The total mass of the instrument is 9.00 kg; the MU flight model mass without thermal hardware is 6.63 kg; and the mass of the IMA flight model is 2.37 kg without thermal hardware. The maximum power consumption is 18 W. The MU envelope is $350 \times 263 \times 288 \, \text{mm}^3$ and for the IMA $287 \times 187 \times 165 \, \text{mm}^3$.

The ASPERA-4 two ENA sensors complement each other. The NPI is designed to provide measurements with relatively high angular resolution but no mass and energy discrimination while the NPD performs mass and energy analysis of the incoming ENAs, but the angular resolution is crude. This approach also gives the necessary redundancy as well as the independent cross-checking that is necessary for such measurements in a new environment.

Severe mass constraints were the main design driver for the ENA sensors. The NPD design using the time-of-flight coincidence and the specially developed START and STOP surfaces optimised for high secondary electron yield, low photoelectron yield, and high UV photon absorption provides high signal to noise ratio and high UV rejection efficiency. It was possible to achieve this performance even within very low mass allocated, i.e., approximately 650 g/sensor including front-end-electronics and the DPU interfacing FPGA but without the high voltage supply and DC/DC convertors. The effective UV suppression scheme as well as velocity and mass resolution were prioritised at the expense of lower angular resolution. In the NPI sensor instead, the priority was given to angular resolution and
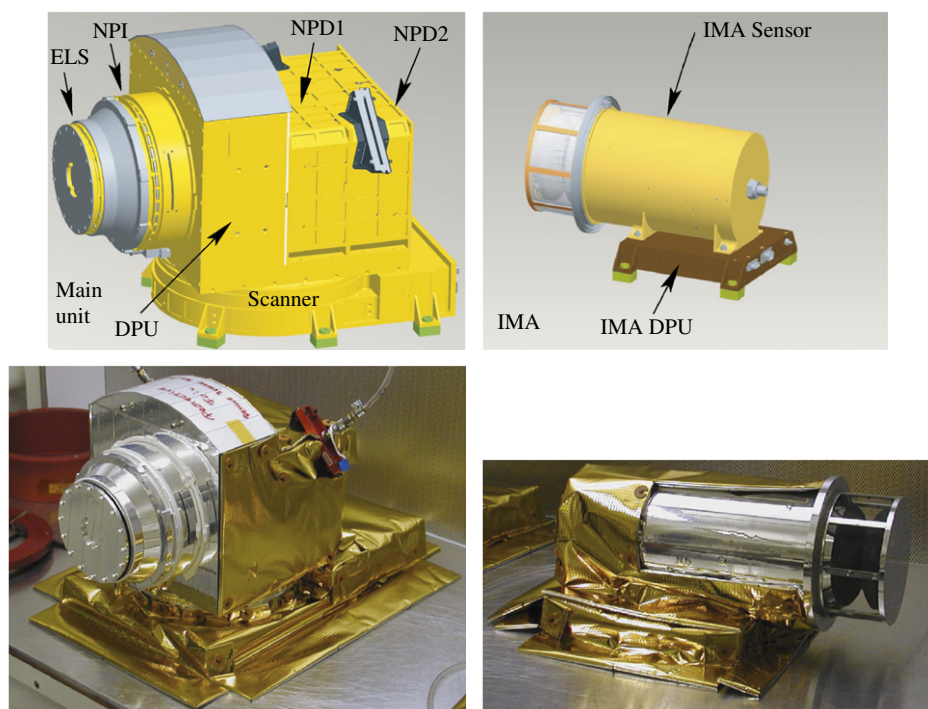
Fig. 1. The ASPERA-4 overall configuration, main unit, and ion mass analyser.

Table 1
The performance of the NPI, NPD, ELS, and IMA sensors

Parameter	NPI	NPD	ELS	IMA
Particles to be measured	ENA	ENA	Electrons	Ions
Energy, keV per charge	≈ 0.1–60	0.1–10	0.01–15	0.01–36
Energy resolution, $\Delta E/E$	–	0.8	0.07	0.07
Mass resolution	–	H, O	–	$m/q = 1, 2, 4, 8, 16, 32, >40$
Intrinsic field of view	$9° \times 344°$	$9° \times 180°$	$10° \times 360°$	$90° \times 360°$
Angular resolution, FWHM	$4.6° \times 11.5°$	$5° \times 30°$	$10° \times 22.5°$	$4.5° \times 22.5°$
G-factor/pixel, cm² sr	2.7×10^{-3}	6.2×10^{-3}	7×10^{-5}	3.5×10^{-4}
Efficiency, %	≈ 1	0.5–15	Incl. in G-factor	Incl. in G-factor
Time resolution (full 3D), s	32	32	32	196
Mass, kg	0.7	0.65 each	0.3	2.4

sensor does not imply any active techniques for UV suppression such as ENA conversion to ions. It was possible to bring the sensor mass down to ca. 700 g that is similar to the NPD mass and includes the front-end-electronics and DPU interfacing FPGA. Reinforcing the NPI structure to provide the stiffness necessary to carry the ELS somewhat increased the overall NPI mass.

The charged particle sensors not only provide characterisation of the local plasma environment but also support ENA measurements in terms of charged particles background and inter-calibrations. The ELS is a standard top-hat electrostatic analyser in a very compact design and high energy resolution. The IMA is an improved version of the ion mass spectrographs TICS/Freja, IMIS/Mars-96, IMI/Planet-B (Norberg et al., 1998), and an exact copy of the ICA (ion composition analyser) instrument that is flying on the Rosetta mission. Since the IMA is not accommodated

on the scanner, electrostatic sweeping is used to achieve $\pm45°$ elevation coverage.

The instrument design, while based on a modular structure, demonstrates high degree of packaging and sharing of internal resources. The instrument DC/DC converters are shared between all five units including the two identical NPD sensors. The DPU mechanical structure also serves as the carrying support for mounting the NPD sensors and the NPI, which in turn is carrying the ELS. The internal walls that separate the DPU, NPI, and the two NPD sensors have been replaced by conductive kapton foils to minimise mass, while maintaining sufficient electromagnetic shielding. Because of the high radiation hardness requirement (30 krad) tantalum point shielding is used. The ELS uses an external metallic conic-shape ring to protect the sensitive electronics. Table 1 summarises the instrument performance.

2.2. The neutral particle imager (NPI)

The ASPERA-4 NPI on Venus Express is a spare model of the ASPERA-3 NPI currently flying on board the Mars Express spacecraft which in turn is a replica of the NPI-MCP sensor developed for the ASPERA-C experiment on the Mars-96 mission and successfully flown on the Swedish microsatellite Astrid launched in 1995 (Barabash, 1995).

In the NPI the charged particles, electrons and ions, are removed by the electrostatic deflection system, which consists of two disks separated by a 3 mm gap (Fig. 2). The 5 kV potential between the grounded and biased disks results in a strong electric field, which sweeps away all charged particles with energies up to 60 keV. Since the integral ENA flux substantially exceeds the charged particle flux for energies greater than 60 keV, this rejection energy is sufficient for satisfactory performance. The disks also collimate the incoming ENA flux over the azimuth angle. Apart from being ON or OFF, the deflection system can be operated in two other modes, alternative mode and sweeping mode. In the alternative mode, the deflection system is turned on and off for one sampling time. This mode is used for more accurate separation between charged and neutral particles entering the system. The deflection system is connected to the high voltage supply via an optocoupler. Regulating the optocoupler reference voltage one can change the deflection voltage performing the sweeping and alternating. In order to reduce the time for discharging of the deflection system disks down to 1 ms, a second parallel optocoupler is used.

The space between the deflection system disks is divided into 32 sectors by plastic (PEEK) spokes forming 32 azimuthal collimators with a field of view of $9° \times 18°$ each.

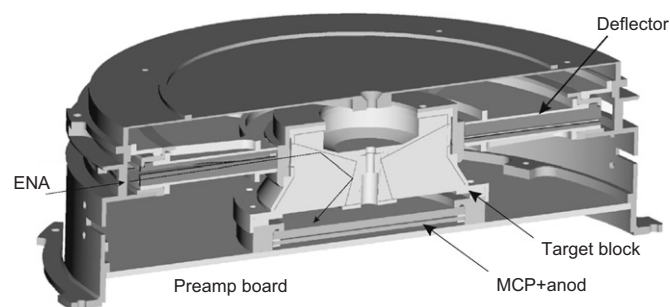Neutrals passing through the deflection system hit a 32-sided cone target at a grazing angle of incidence of 20°. On impact with the target block the incident neutral can either be reflected, produce secondary particles, or both. The secondaries can be both ions and electrons. A 56 mm diameter PHOTONIS MCP stack in chevron configuration followed by a 32 sector anode detects the particles leaving the target. The signal from the MCP gives the direction of the primary incoming neutral. The MCP operates in ion mode with a negative bias of slightly more than -2.2 kV applied to the front side and thus detects (a) sputtered positive ions of the target material, (b) positive ions resulting from ionising of the primary neutrals, and (c) neutrals reflected from the target surface. In order to improve the angular resolution and collimate the particles leaving the interaction surface, 32 separating walls are attached to the target forming a star-like structure. This configuration allows the entering particles to experience multiple reflections and reach the MCP. NPI covers 4π using one scanner scan (except a fraction blocked by the spacecraft body) and produces an image of the ENA flux distribution in the form of an azimuth $\times$ elevation matrix. The direction vector of 32 elements is read out once every 62.5 ms. Two sectors centred around the spin axis and looking toward the spacecraft body are blocked intentionally to provide monitoring of the MCP assembly dark counts. This space is also used for the ELS sensor harness. The internal views of the NPI sensor is given in Fig. 3.

A calibration of the NPI sensor was preformed to characterise the MCP-saturation bias, dark count level, angular response in elevation and azimuth, and efficiency. One sector (number 4) was thoroughly investigated, and a scan with the calibration beam in the central plane of all sectors was used to find the relative response of the other 31 sectors. The calibration was performed using an ion beam as a particle source. This is equivalent to using an ENA beam, since particles "forget" their initial charge state when interacting with the surface of the target block.

Fig. 4 is the efficiency of the NPI measured with H_2O^+ ions and protons in the beam for different MCP bias and energies. The efficiency was measured in sector 4 with the neighbouring sectors mechanically blocked. For the MCP operating bias 2.2 kV the efficiency for solar wind energies ($\sim$1 kV) is around 5×10^{-4}. Fig. 5 shows a scan in the central plane of all sectors over a wide parallel beam
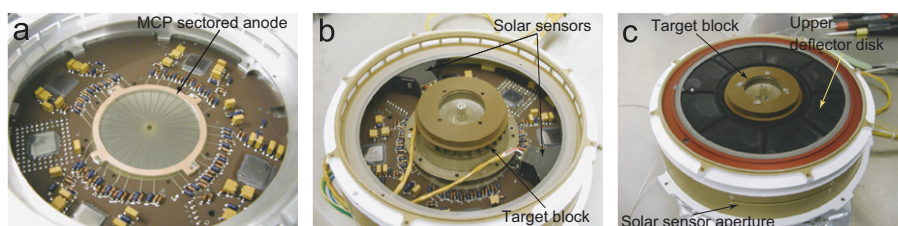

Fig. 2. Cut-away view of the NPI sensor.

Fig. 3. NPI integration: the sectioned anode (a), target block installed (b), and deflection system mounted (c).

of 5 keV protons. This measurement was performed to calibrate out the relative sensitivity of the sectors, which varies significantly. Since the sector angular (polar–azi-

Fig. 4. The efficiency of sector 4 with neighbouring sectors mechanically blocked.

muth) response function should be included in the ENA image inversion models it was measured and analytical fits were produced. The upper panels of Fig. 6(a) show the measured data and response function and the lower panels show a polynomial fit to the response.

An important issue in the NPI design is the coating of the target block for suppressing UV photon fluxes, which enter the instrument and produce the UV background in the measurements. NPI uses the same coating as in the experiments PIPPI (prelude in planetary particle imaging) on board Astrid-1 and ASPERA-C on board MARS-96, namely, DAG 213, a resin-based graphite dispersion. This is similar to Aquadag, which is a graphite dispersion in water. The DAG 213 paint was applied on the finished aluminium surface by air-brush in three layers. The details of the surface preparation as well as related laboratory studies can be found in Barabash (1995). The coating demonstrated satisfactory performance in the PIPPI experiment flown in the Earth's magnetosphere (C:son Brandt et al., 2000). To determine the target block UV suppression the NPI was calibrated against hydrogen Lyman-α photons ($\lambda = 121.6$ nm). The calibration philosophy was similar as that of the particle calibration in that

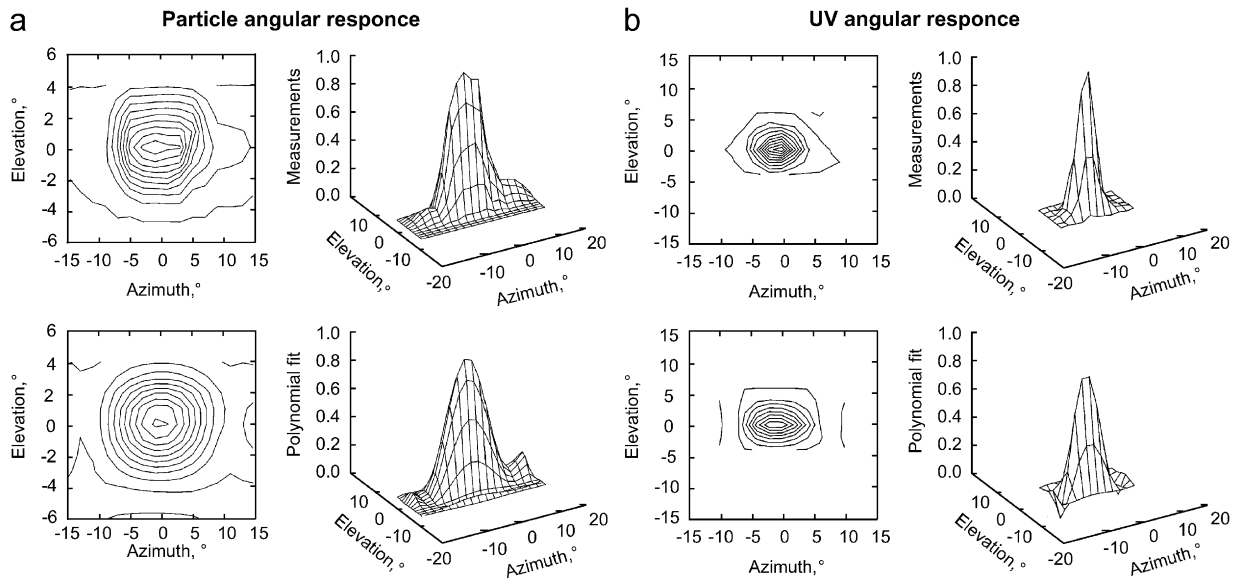Fig. 5. Scan through the central plane of the sectors.

Fig. 6. (a) Full angular scan with sector 4 in the particle beam (protons). The lower panels show a polynomial fit. (b) Full angular scan with sector 4 in a UV photon beam (Lyman-α). The lower panels show a polynomial fit.

the response of one sector (number 4) was fully characterised then a relative measurement was made for the other sectors.

During calibrations conducted at the University of Arizona the UV-intensity in the beam was continuously monitored by an absolutely calibrated channeltron. The maximum intensity measured was 10^7 photons per second into the aperture of the NPI. The measured count rate was ~30 counts per second, which corresponds to a UV suppression efficiency of $10^7/30 \approx 3 \times 10^{-5}$. This is somewhat higher than what was previously reported by Barabash (1995).

The intensity measurement is important to understand the NPI UV response. If we know that the response is more or less linear within certain intensities we can scale the response against what is present in space to determine the photon related background. Due to an unstable beam only three points on this curve were obtained. The NPI count rates for the respective beam intensities are plotted in Fig. 7.

It is important to know what the UV-response is at different incident angles to an NPI aperture. An angular scan could reveal if there are any reflections off the deflection plates or the spokes in the electrostatic deflection system. The angular scan was made with respect to the aperture plane of the NPI (sector 4). We should thus expect not to see any counts in any other sector than number 4. If we do, this must be a result of internal reflections since all photons from the beam are directed into the centre of sector 4 for all angles. The result of the angular scan is in Figs. 6(b), and Fig. 7(b) shows the sum of all counts during the angular scan in all sectors. The count rate in the sectors 3 and 5 is at around 10% of that in sector 4. To ensure that there are no reflections from the spokes of sectors other than the centre, a translation
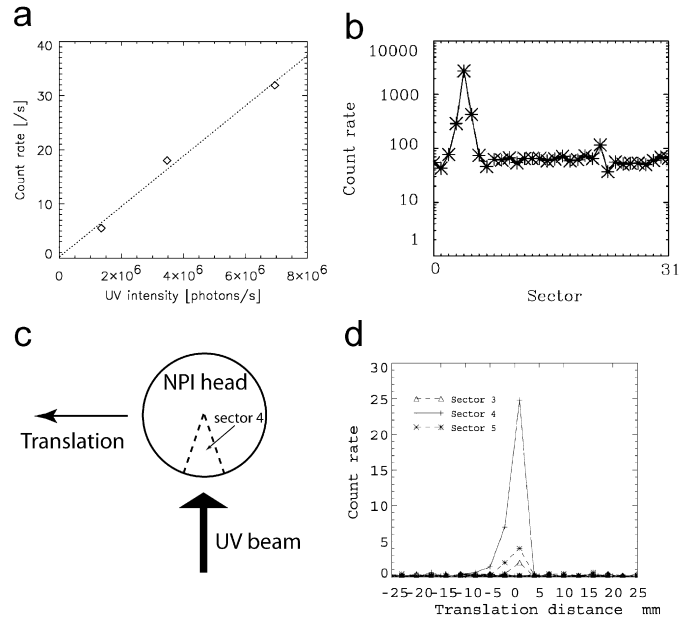

Fig. 7. (a) NPI sensitivity to UV intensity. (b) Total count during angular scan of sector 4 with UV beam. (c) Translation measurement set up. (d) Translation measurement results.

measurement was made. Sector aperture number 4 was centred in the UV beam direction and the NPI was horizontally translated according to Fig. 7(c). The space in the tank limited the translation to less than the full diameter of the NPI. However, reflections from aperture spokes further away than the translation range is highly unlikely as it would require a multitude of reflections to reach the target block. The resulting counts are in Fig. 7(d). It shows that there are not significant counts in any sector other than 4.
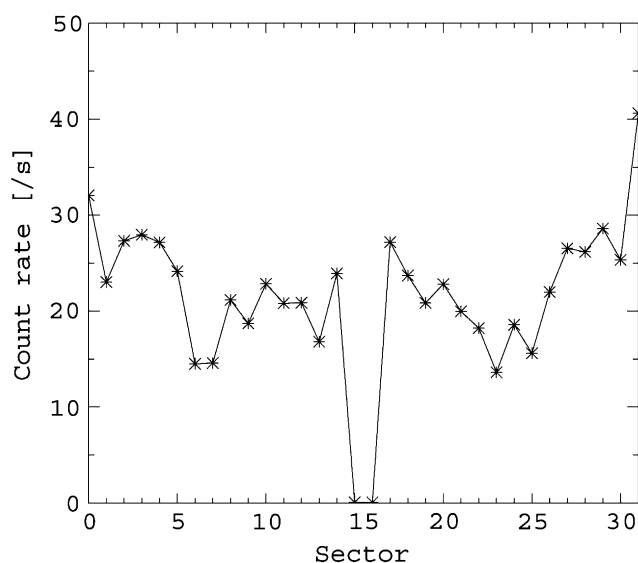
Fig. 8. The relative response of all sectors to the UV photons (Lyman-α). The measurements are taken with the UV beam centred on the aperture of each sector.

Fig. 9. Three-dimensional view of the NPD principal components.

The relative response of other sectors was measured with the beam centred in the centre of each sector aperture. The beam intensity-normalized result is shown in Fig. 8.

2.3. The neutral particle detector (NPD)

The NPD sensor consists of two identical detectors, each of which is a pinhole camera. Fig. 9 provides a conceptual view of one NPD detector.

In each detector the charged particles, electrons and ions, are removed by a deflection system, which consists of two 90° sectors separated by a 3.0 mm gap. In the normal operational mode the 10 kV potential (±5 kV) applied to the sectors and the resulting strong electric field sweeps away all charged particles with energies up to 70 keV. The deflector also collimates the incoming ENA flux in the elevation angle. The collimated ENA beam emerging from the 3.0 × 4.5 mm pinhole hits the START surface under a 15° grazing angle causing secondary electron emission. By a system of collecting grids, the secondary electrons are transported to one of two MCP assemblies that give the START signal for TOF electronics.

Depending on the azimuth angle, the collection efficiency varies from 80% to 95%. The incident ENAs are reflected from the START surface near-specularly. Since the charge state equilibrium is established during the interaction with the surface, the emerging beam contains both the neutral and ionised (positive and negative) components. To increase the total efficiency, no further charge separation is made.

As proven by the ion tracing, there is very little disturbance to the reflected atomic ions leaving the START surface with an energy above 80 eV, introduced by the START electron optics. Fig. 10 shows the results of electron and ion ray-tracing in the START assembly electron optics.
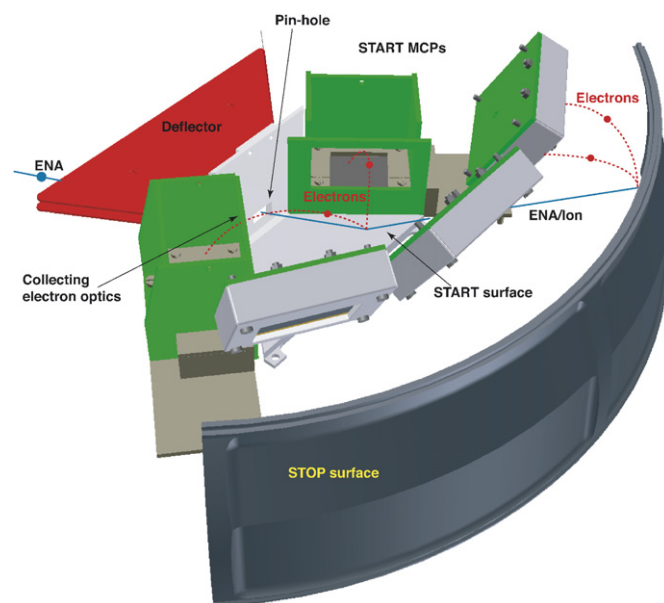
Therefore particles of all charge states, i.e., negative, neutral, and positive, will impact the second surface, the STOP surface, and again produce secondary electrons, which are detected by one of the three MCP assemblies giving the STOP signal. The time-of-flight over a fixed distance of 8 cm defines the particle velocity. Three STOP MCPs also give crude angular resolution over azimuth within 90° acceptance angle. Since the secondary electron yield depends on mass for the same velocity, the pulse height distribution analysis of the STOP signals provides the estimation of the ENA mass. Each event is stored in the array STOP MCP charge × time-of-flight × direction. The array is accumulated over the sampling time 1.0 s.

Fig. 11 shows a cross-section of the NPD sensor and its main elements with an ENA trajectory shown in blue. Fig. 12 shows the views of the flight model of the NPD sensor. Each sensor has an acceptance angle of 90°. Two identical sensors are built in a package installed on the scanning platform providing 180° scans and thus organising 2π coverage. Fig. 13 shows the two flight NPD sensors during installation into the ASPERA-4 instrument with apertures covered by red-tagged covers with nitrogen purging tubes connected.

The selection of the START and STOP surfaces was the most challenging part of the NPD development. Extensive studies have been performed at University of Bern (Jans, 2000) and Brigham Young University (USA) to optimise the performance of the surfaces. The START surface must satisfy a number of requirements, namely, high secondary electron yield, high UV absorption even at grazing angles, high particle reflection coefficient, low angular scattering, and low photoelectron yield. The STOP surface must
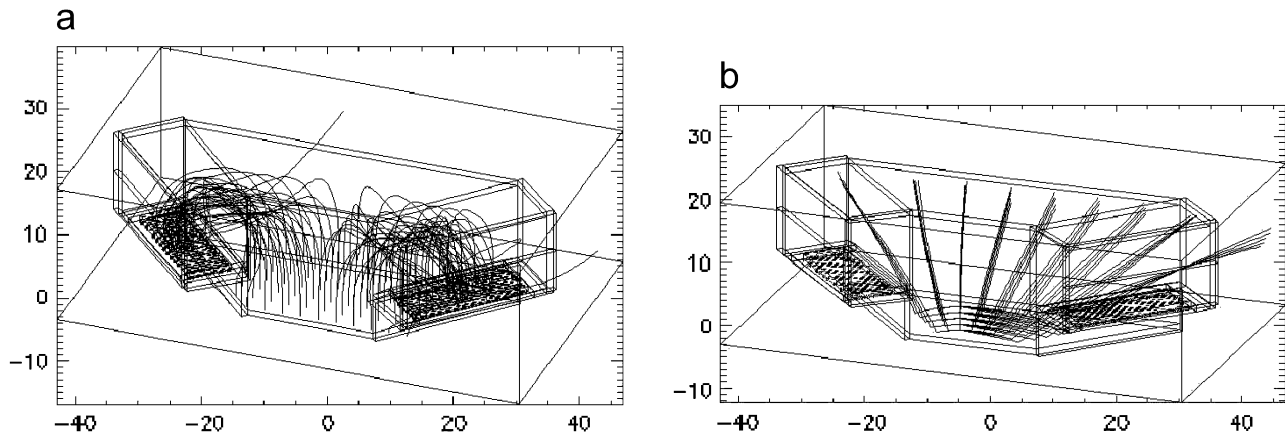
Fig. 10. Ray-tracing of electron (a) and 80 eV ion trajectories (b) in the START assembly optics.
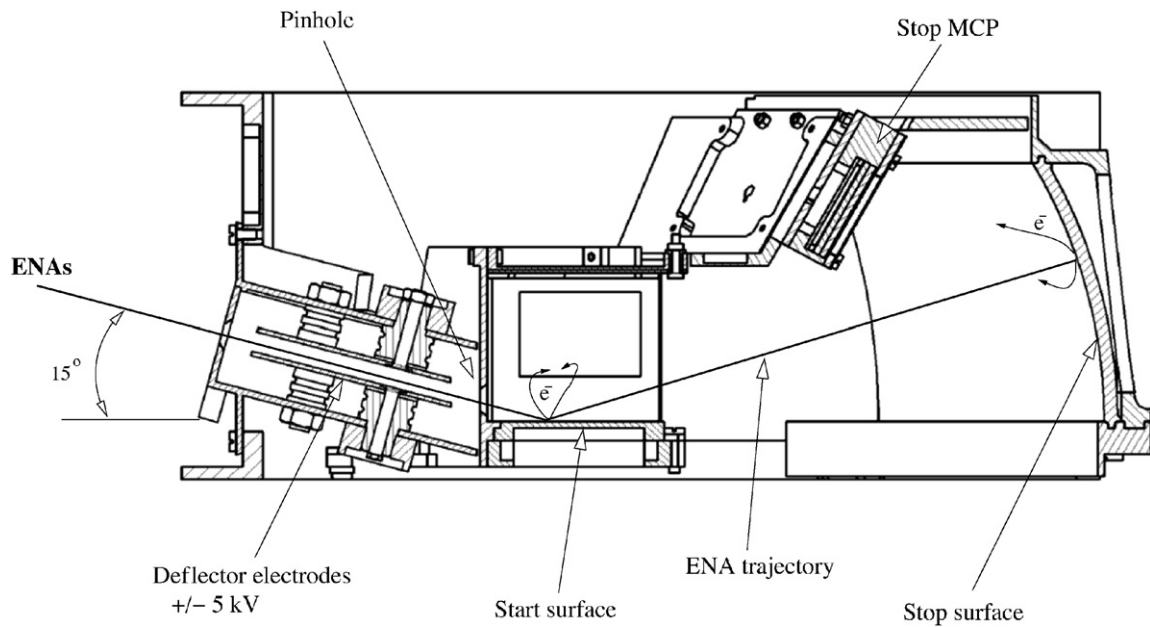

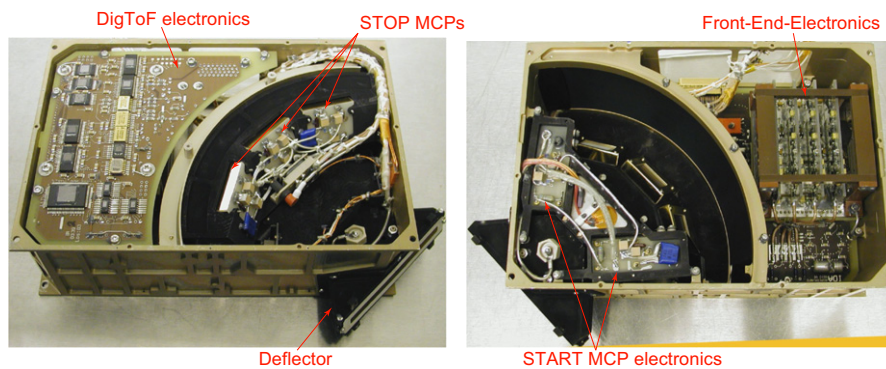Fig. 11. Cross-view of the NPD sensor.

Fig. 12. Top and bottom view of the flight model of the NPD sensor.

satisfy similar requirements namely, high secondary electron yield, high UV absorption, and low photoelectron yield.

For the START surface we chose a multi-layer coating composed of thin layers of Cr_2O_3 and thicker layers of MgF, and topped with a thin layer of WO_2. The coating is
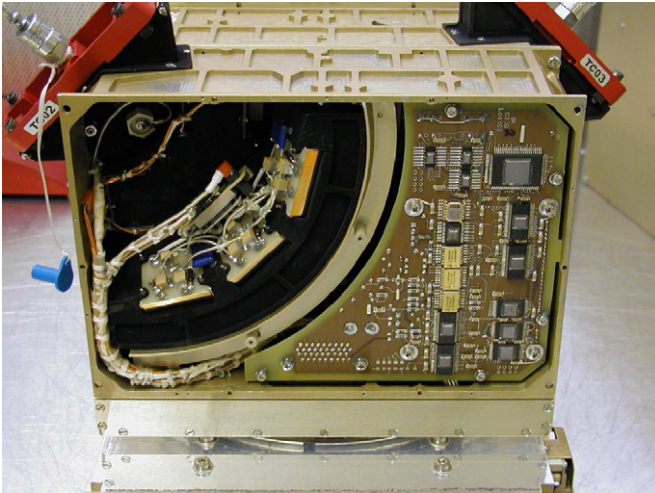
Fig. 13. The flight model of the NPD sensor during installation.

Fig. 14. NPD TOF spectra of proton beams at different energies.

Fig. 15. NPD TOF spectra of H_2O beams at different energies.

optimised for the absorption of the 121.4 nm line at the $15°$ incident angle. The reflection coefficient reached was about 30%, a factor of 2 lower than the uncoated surface. The coating is applied on a titanium substrate polished down to 100 Å roughness.

The STOP surface is graphite (roughness around 100 nm) covered by a MgO layer of about 500 nm. MgO has a very high secondary electron yield (Cazaux, 1993). Since MgO is an insulator with a band gap of 7.8 eV (Deutscher et al., 1999), only photons with wavelengths $\lambda \leqslant 160$ nm can release a photoelectron, thus resulting in a low photoelectron yield. The graphite base of the STOP surface serves to efficiently suppress any photon that passes through the MgO coating. A lot of effort has been spent to increase the stability of the MgO coating against moisture. It was established that polishing the graphite substantially improves the stability and possible increases in air humidity during storage and pre-launch operations does not present any problems for the surface performance. Also, the MgO film thickness was optimised for that purpose. In summary, both surfaces are reasonably stable in ambient air and do not require special protection measures other than the typical measures taken for storing MCPs.

In-flight determination of the UV sensitivity of the NPD sensors of ASPERA-3 on the Mars Express mission using known fluxes of Ly-α backscattered from the interstellar gas and the light of nearby UV-bright stars (Galli et al., 2007) gives a UV response in the TOF channel of

$$C_{TOF} = \left(\frac{I}{2.86 \pm 0.6} \right)^2, \qquad (1)$$

where C_{TOF} are the counts per second in the TOF spectrum and I is the Ly-α intensity in kRa. The UV suppression of the NPD sensor also benefits from the coincidence measurement (the time-of-flight measurement); the single rates arising from incoming UV photons are much higher,
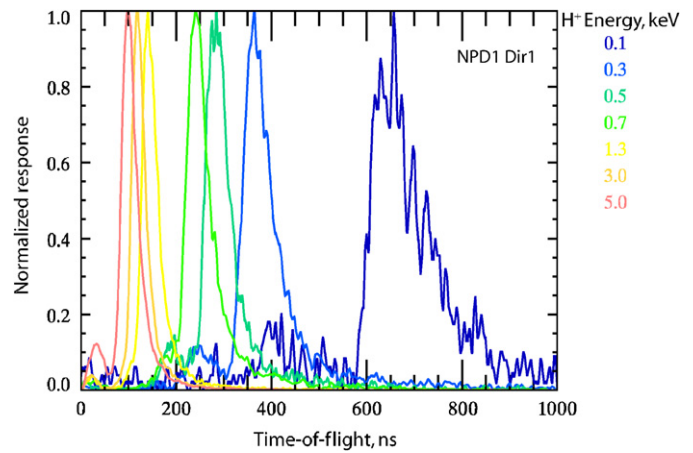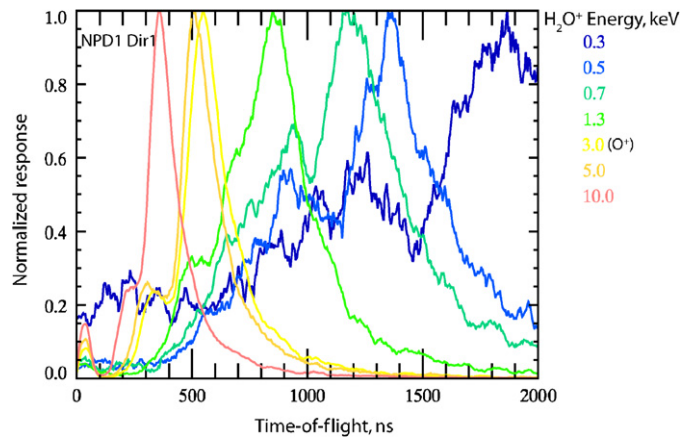
for the START a few $10^4 s^{-1}$ and for the STOP a few $10^3 s^{-1}$ are registered.

The NPD calibrations included determining the efficiency, geometrical factor, angular response and energy resolution. The calibration results fully correspond to the specified performance. Since charge-equilibrium establishes over just a few Å at the particle-surface interaction, ion beams can be used for calibrations of ENA sensors. Fig. 14 shows the TOF distributions for a proton beam at different energies (colour coded) in the energy range from 0.1 to 5.0 keV. The displacement of the peaks from the exact energy of the incident particles reflects the energy loss of 33%, which is independent on energy. The full width at half maximum (FWHM) is about 80%. Fig. 15 shows the TOF distributions for H_2O^+ ion beams of different energies covering the energy range from 0.3 to 10.0 keV. The energy losses are the same as for the proton beams.

Fig. 16 shows calibrated dependence of the measured TOF on the incoming particle energy for protons and H_2O^+ ions. The dashed lines show the theoretical dependence corresponding to the 33% energy loss in the START surface. The water molecule ions used in the
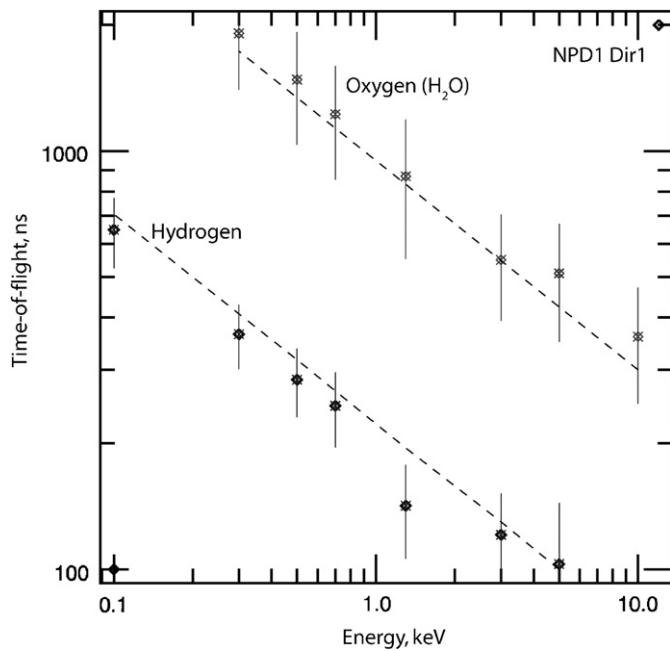
Fig. 16. Time-of-flight measurements for different masses as a function of energy. The dashed lines give the theoretical dependence corresponding to 33% energy loss.
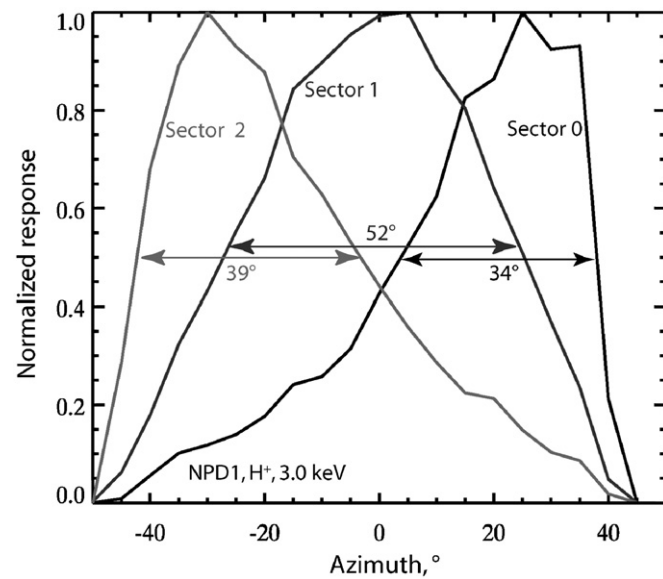

Fig. 17. The angular response of the NPD sensor over azimuthal.
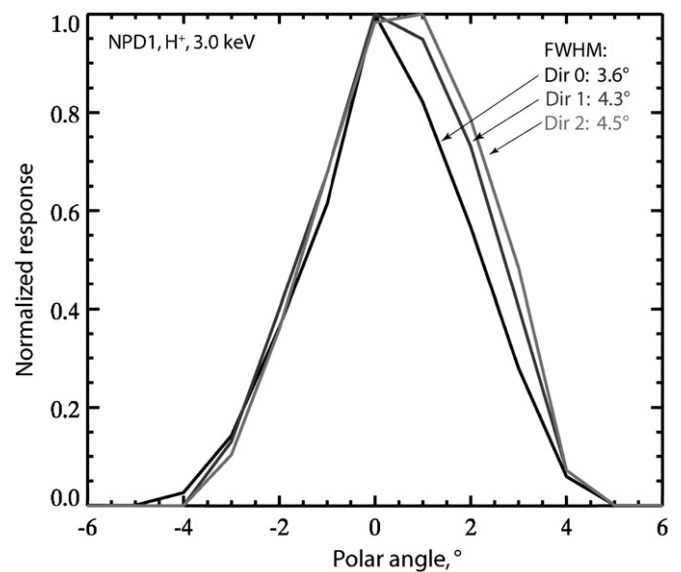

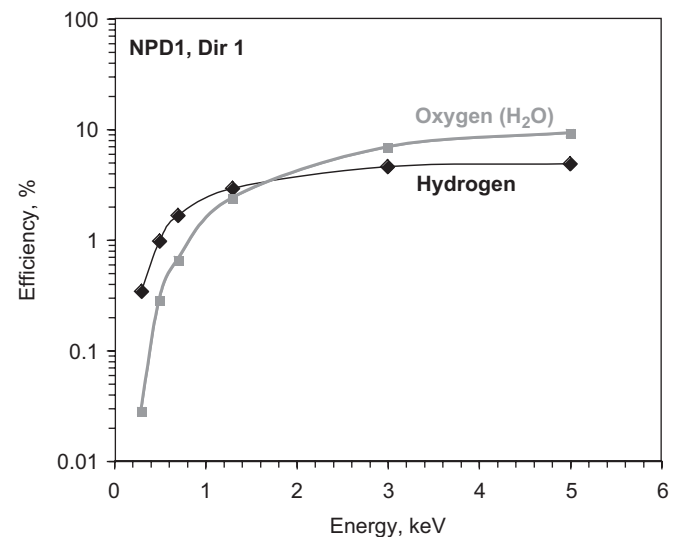Fig. 18. The angular response of the NPD sensor over elevation.

Fig. 19. NPD sensor absolute efficiency.

calibrations break up during the impact, but the residual components carry the same initial velocity corrected for the energy loss in the target. Therefore, water can be used to calibrate the response of the instrument to oxygen beams. Since the TOF for oxygen with an energy below 2 keV is longer than the TOF corresponding to slowest protons at around 100 eV TOF measurements alone can be used to identify the particle mass at least in the low energy range.

Fig. 17 shows the NPD angular response over azimuth for a 3 keV proton beam for the three STOP sectors. The red line shows the response of the central sector and the green and the black lines show the side sectors. Fig. 18 shows the sensor angular response over the elevation. The FWHM over azimuth varies from 52° for the central sector to 35° and 37° for the two side sectors, respectively. Over elevation the FWHM is 4.5° for all directions.

Fig. 19 shows the absolute efficiency of the NPD sensor as a function of energy. The blue line corresponds to the incident proton beam and the red line corresponds to the H_2O^+ beam.

As is seen in Fig. 19 the efficiency is more than 11% for H_2O ENAs at 6 keV. For the H ENA the efficiency reaches 7%. Up to a certain energy the efficiency increases with energy, corresponding to an increase of the secondary electron yield. At the energy where the yield reaches unity the efficiency levels out (approximately 3 keV for protons
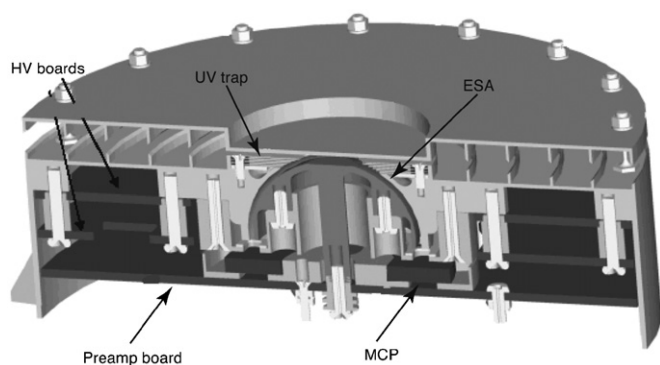
Fig. 20. Cut-away view of the ELS sensor.

and 6 keV for oxygen). At energies below 1 keV, the efficiency is around few percent.

2.4. The electron spectrometer (ELS)

The electron spectrometer (ELS) sensor represents a new generation of ultra-light, low-power, electron sensor (Fig. 20). It is formed by a 17° spherical top-hat electrostatic analyser and a collimator system with the radii of the inner and outer hemispheres equal to 14.9 and 15.9 mm, respectively. Particles can enter the aperture at any angle in the plane of incidence. Electrons are then deflected into the spectrometer by applying a positive voltage to the inner hemisphere. The electrons hit an MCP after being filtered in energy by the analyser plates. A spectral measurement is achieved by stepping the plate voltage.

Electrons with energies up to 20 keV/q are measured, with a maximum time resolution of one energy sweep (consisting of 128 steps) per four seconds. There are 16 anodes behind the MCP, each anode defining a 22.5° sector and each connected to a preamplifier. The ELS sensor is mounted on the ASPERA-4 scanner platform, on top of the NPI sensor, in such a way that the full 4π angular distribution of electrons will be measured during each platform scan (a fraction of the solid angle is blocked by the space craft). Depending on the mode of operation a sample rotation scan takes 32, 64, or 128 s.

The ELS was designed to be solar blind so that it may operate in exposure to direct sunlight. This has been achieved using two UV reducing mechanisms and one secondary electron suppression technique. UV is minimised through the use of a series of light baffles in the ELS collimator and a series of UV light traps at the entrance to the spherical deflection plates. Secondary electrons are reduced by the addition of a special coating, based on a modified Ebanol-C process, which is included through out the deflection surface, light trap, and collimator system (Johnstone et al., 1997).

There are two small differences between the ASPERA-3 (on board Mars Express) and ASPERA-4 ELS units. One is the inclusion of an outer cylindrical 2 mm thick aluminium shield, which was added to prolong ASPERA-4

ELS operation in the harsher radiation environment of Venus. The other is an offset of the symmetry axes of the ASPERA-4 ELS deflection plates outside the 1% design specification. This happened because the ASPERA-4 ELS, as the refurbished Mars Express flight spare, was actually built earlier than the ASPERA-3 ELS, and therefore did not have the advantage of a critical improvement in the fabrication process that ensured that the stringent 1% requirement was achieved. The misalignment results in differences in instrumental properties as a function of the anode sector position, which will be illustrated in the calibration results discussed below.

The ASPERA-4 ELS was calibrated at Mullard Space Science Laboratory, University College, London. The calibration facility (Johnstone et al., 1997), which is based on the technique described by Marshall et al. (1986), provides a wide area photoelectron beam at energies ranging from a few eV to 15 keV with variable beam intensities from a few Hz to several MHz. The system is fully automated facilitating calibration scans over the complete range of polar and azimuth angles at several instrument voltage settings both for the analyser as well as the MCP. A flexible data acquisition system was integrated into the automation to provide simultaneous measurements from the 16 preamplifier channels, coordinated with the instrument position and voltage settings. Before performing the instrument calibration, a profile of the beam output is recorded at each of the calibration energies by means of a channeltron mounted on an $X–Y$-table. A typical profile at 30 eV is shown in Fig. 21. During calibrations, the channeltron is mounted as close as possible to the instrument aperture in order to provide a constant reference to the beam intensity. Due to the mechanical imperfections of the instrument mentioned
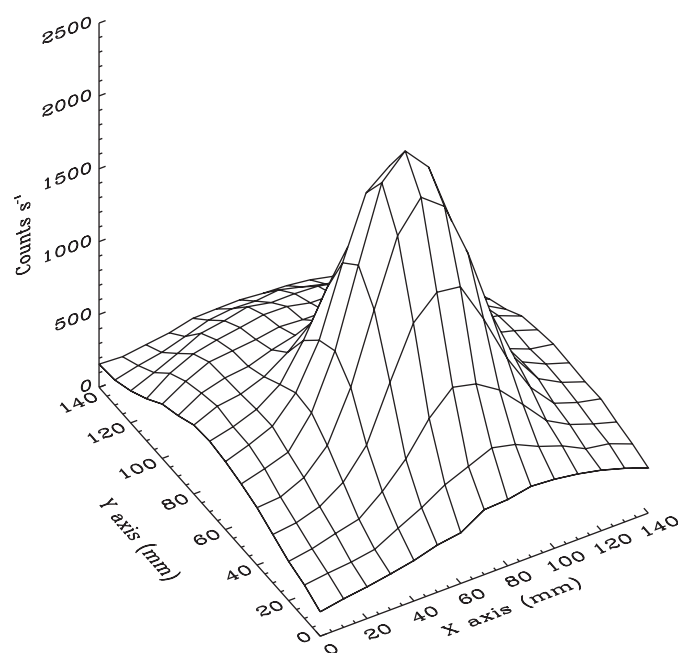

Fig. 21. Profile of 30 eV electron beam prior to ELS calibration.

above, the laboratory calibrations were critical for defining the instrument response.

The instrument has two operational voltage ranges for the energy sweeps as described later and hence, tests were carried out at several energies in both ranges to cover ±180° in polar and ±3° in elevation. Fig. 22 is a typical plot of the voltage–angle scans carried out over the 16 anodes at 30 eV in the lower range. Fig. 23 is a plot of the k-factor across the 16 anodes giving an average value of 11.33. Although this is higher than the design value of 7.5 due to the mechanical imperfections, the variation across the anodes is less than 5%, allowing the instrument response to be made good with the calibrations with small errors. The imperfections result in a lower geometric factor

but have the advantage of increasing the maximum energy acceptance of the instrument. The calibrations also establish the MCP operational levels for flight which are found to be 150 V higher for the ASPERA-4 compared to the ASPERA-3 unit. This is possibly due to an MCP with a lower intrinsic gain and/or due to a higher electronics threshold for the readout electronics. Finally, the UV rejection ratio of the analyser was also tested using a Lyman-α UV source (Alsop et al., 1996).

The ELS unit has a self contained, dual range, linear high voltage power supply. The first power supply range is from 0 to about 20 V (about 150 eV) and has 4096 possible settings. The second power supply range is from 0 to 2800 V (about 20 keV) and also has 4096 possible settings.
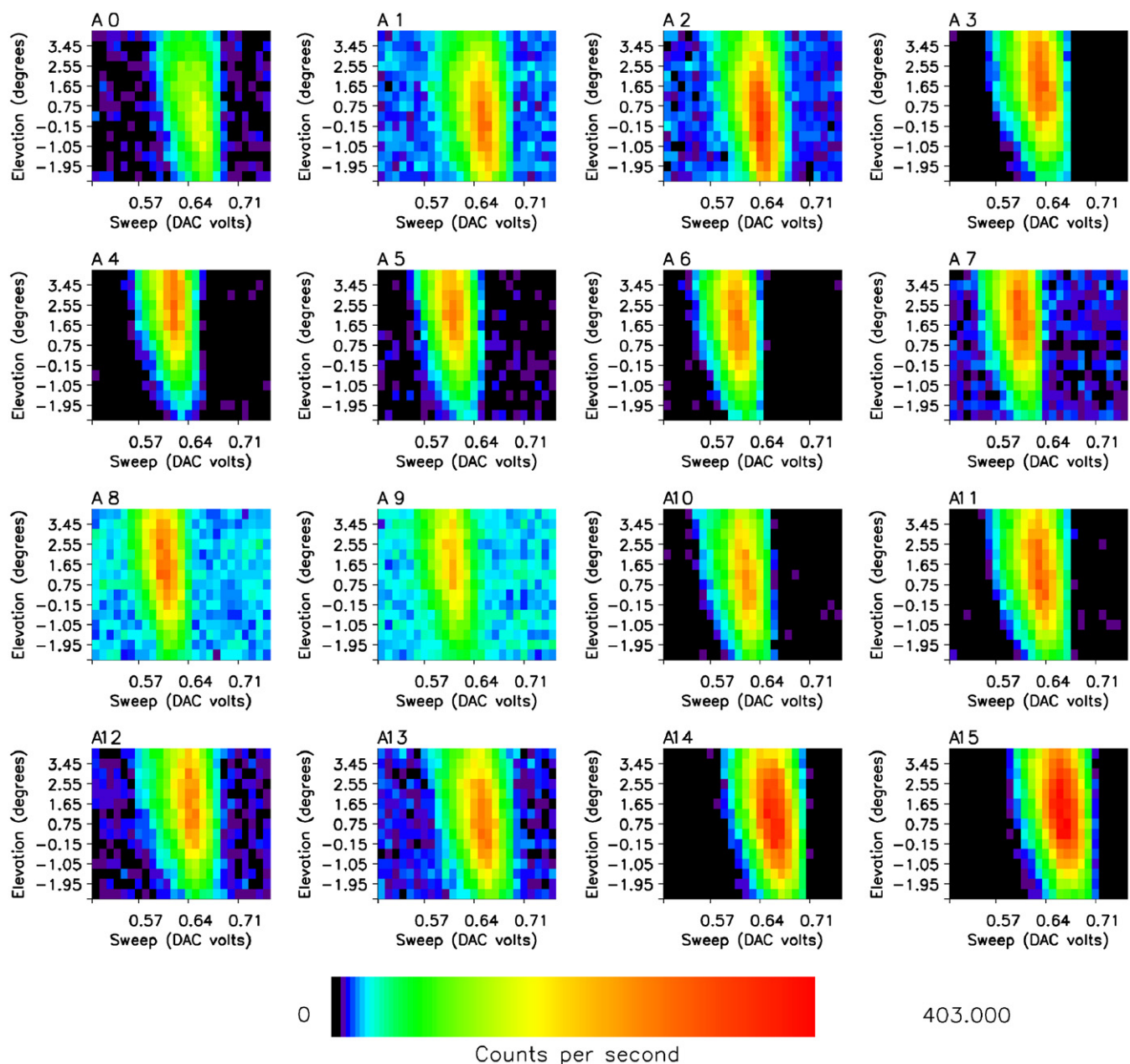

Fig. 22. Spectrograms of elevation angle versus the applied voltage on the inner hemisphere for a 30 eV beam.
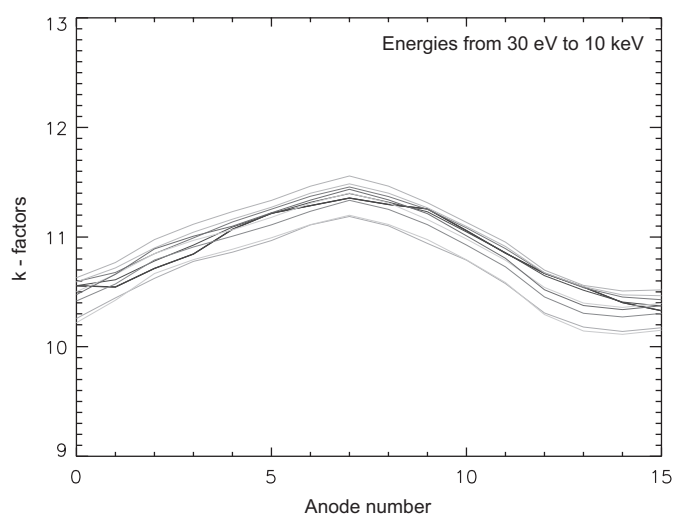
Fig. 23. Plot of the *k*-factor across the 16 anodes.

Fig. 24. Photoelectron spectrum from the Mars ionosphere.

The ELS sweep is fully programmable within the constraint of the maximum decay rate of 32 steps/s. On any given step, the deflection plate voltage is held constant during a minimum of 28.125 ms used to accumulate electrons. There is a minimum of 3.125 ms of data latency between energy steps for transition.

In order to obtain high resolution measurements of the energy spectrum, the power supply may be operated in an oversampling mode, which, when combined with the knowledge of the instrumental response function, increases the number of measurement points per energy interval over a reduced energy range. Measurements in this mode are shown in Fig. 24, which shows a clear resolution of the CO_2 photoelectron peaks, characteristic of the Martian atmosphere.

2.5. The ion mass analyser (IMA)

The IMA (Fig. 25), is an improved version of the ion mass spectrographs TICS (Freja, 1992), IMIS (part of ASPERA-C, Mars-96, 1996), and IMI (Planet-B, 1998) (Norberg et al., 1998). It is an exact copy of the ICA instrument that is on its way to comet 67P/Churyumov-Gerasimenko on board the Rosetta spacecraft.

The principal diagram of the instrument is shown in Fig. 26. Ions enter the analyser through the external grounded grid. Behind the grid there is a deflection system whose purpose is to vary the incident polar angle of particles (shown in Fig. 26 as trajectories 1, 2 and 3). The deflection angle depends on the voltage applied to the deflector electrodes and lies within the ±45° from the equatorial plane of the instrument. Fig. 27 shows the instrument polar angle response as a function of the deflector voltage. Then ions pass through the top-hat electrostatic analyser, which selects only the given particle energy according to the interplate voltage. Since the top-hat analyser has a full 360° cylindrical symmetry, the azimuthal range (in the plane perpendicular
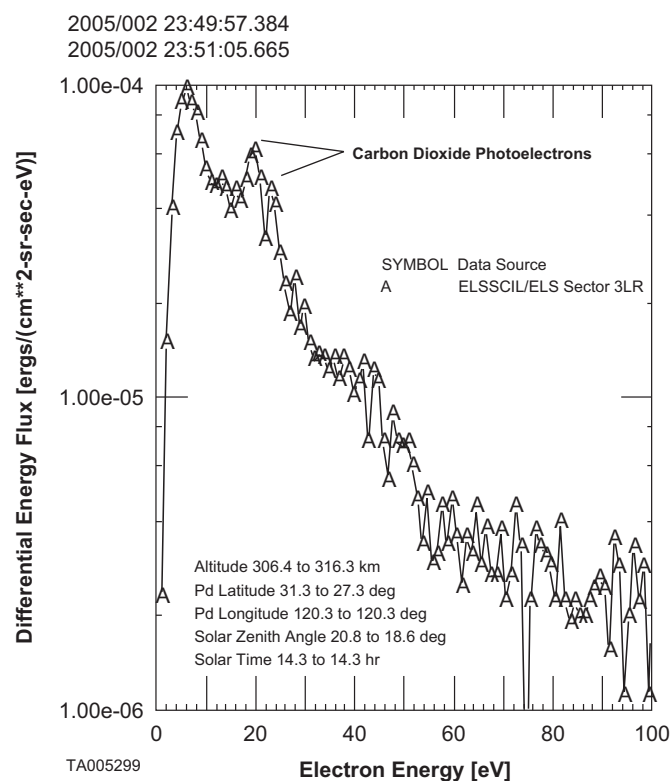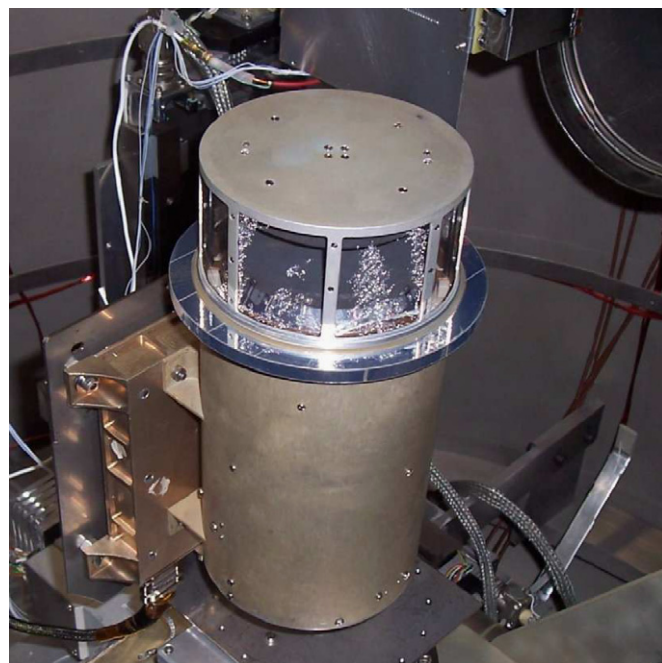

Fig. 25. The IMA sensor in the vacuum chamber.

to the symmetry axis) of the instrument is 360°. The parallel incident ion beam is focusing in the vicinity of the exit of the top-hat analyser. Thus the particle position at the top-hat analyser exit codes its azimuthal angle. Then the ions pass through the magnetic separation section. The cut of this
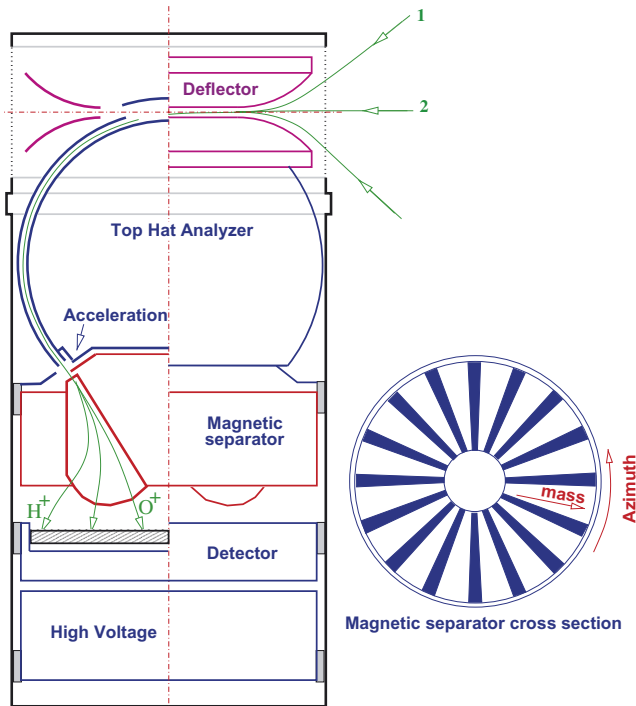
Fig. 26. Cross section of the sensor (left) with examples of the ion trajectories, and magnet separator (right).

Fig. 28. Radial profiles of a few mass peaks. The particle energy is 1250 eV and the post acceleration voltage is −2150 V.
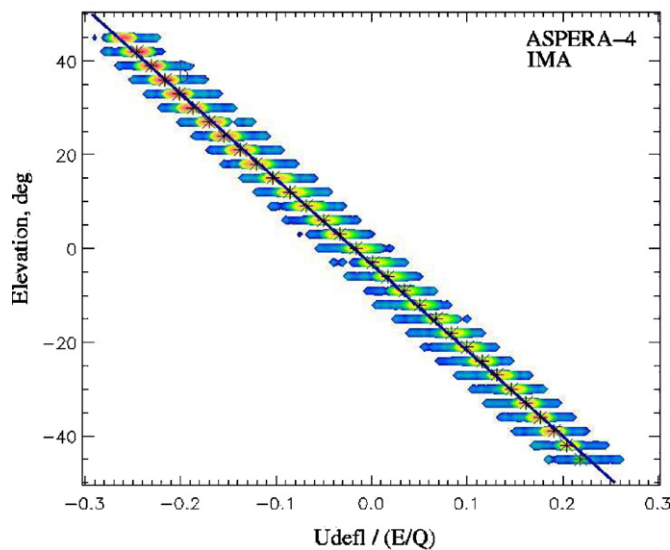

Fig. 27. Colour coded instrument response as a function of polar (elevation) angle and deflector voltage normalised to the ion energy.

section in the azimuthal plane is shown in the right panel of Fig. 26. The magnets are shown as black sectors. Sixteen gaps between the magnets correspond to 16 azimuthal sectors of the instrument of 22.5° each. The radial deviation of the ion trajectories at the exit of the magnetic field region corresponds to the particle velocity per charge. Since exiting the electrostatic analyser particles have the same energy per charge value, the radial deviation codes the ion mass.
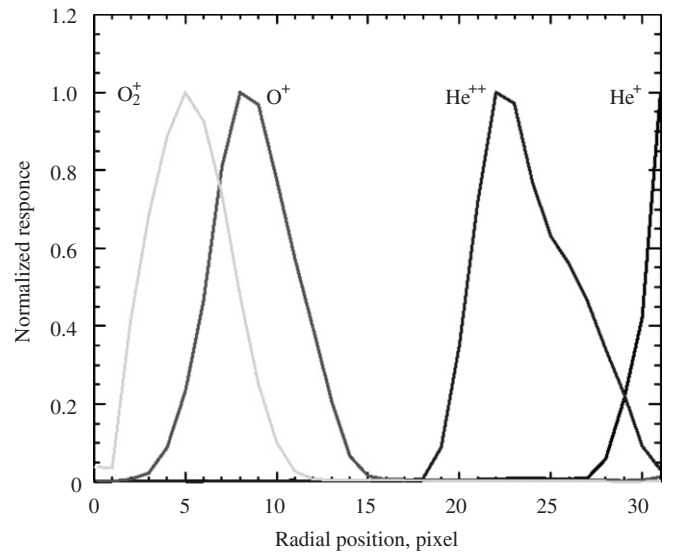
The particles are registered by an MCP with a position sensitive anode. The anode resolves 32 bins in the radial position and 16 azimuthal sectors. An example of the detector response is shown in Fig. 28.

To provide the possibility to measure light ions at low energies, ions, such as H^+ which have too small gyro-radius to reach the MCP, can be accelerated between the top-hat analyser exit and the magnetic separator entrance. Fig. 28 shows the 1 keV particles distribution over the detector surface when the acceleration level is −2150 V. Protons reach the MCP only partially for this post acceleration level. With an acceleration of 3615 V protons hit the detector at least down to an energy of 300 eV. From Fig. 27 one can see that polar angle resolution for constant deflector voltage is about 6°. Fig. 29 shows the azimuthal response of the instrument.

Besides the ion analyser and position sensitive detector The IMA sensor also includes a high voltage unit that provides all sweep voltages and MCP bias, and an IMA DPU. The IMA DPU, which is built around the 16-bit MA31750 processor from Dynex, controls analyser voltages, reads out and accumulates the position information for each detector event, and forms telemetry packets. The hardware operation mode is fixed. The fastest changing parameter is the particle energy. It sweeps from 30 keV down to 10 eV over 96 logarithmically equidistant steps. The exposure time on each energy step is 125 ms. During this time interval 16 radial position spectra (32 points) corresponding to 16 azimuthal sectors are accumulated. After each complete energy sweep the instrument changes the polar angle of the field of view. The polar angle is scanned from −45° up to +45° over 16 steps. The total time to complete a full 3D spectrum is 192 s. This spectrum consists of 32 radial (mass) points ×16 azimuthal sectors ×96 energy steps ×16 polar angles. The data processing
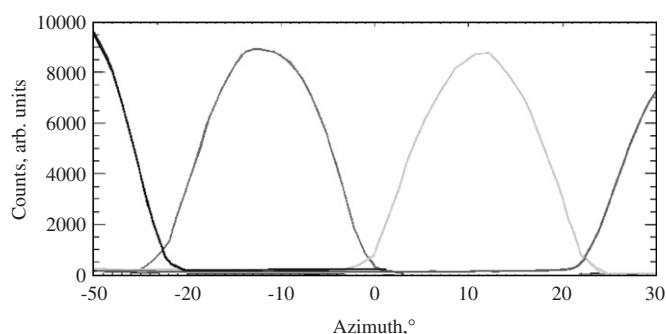
Fig. 29. Azimuthal response for selected sectors.

includes three stages: (1) logarithmic compression of the count values; (2) integration (if necessary) over polar angles, and/or azimuthal angles; and (3) RICE compression of the final spectrum. The processing mode is set by Telecommands (TC) or chosen automatically according to the TM rate limitations. The acceleration level is also commandable. Only three values of acceleration are available: 0, −2150 and −3650 V.

2.6. The digital processing unit (DPU)

The ASPERA-4 DPU mechanically includes two boards: the DPU board itself and a housekeeping (HK) board. These are connected together with the sensor control electronics and the power supply via a common bus system with 8 address and 16 data lines besides control, analog and power supply lines.

The DPU is built around a 16-bit processor MA31750 from Dynex with 12 MHz system clock frequency and an Actel field programmable gate array (FPGA) RT54SX32S, which implements memory management, watchdog functions and the serial spacecraft interface protocol. The software runs inside a 128 kbyte RAM, organised in 2 banks of two 32 kbyte static memory chips each. On power-up, a two times 16 kbyte bipolar PROM (HARRIS) is activated with a boot loader, which transfers the complete PROM contents into the RAM, changes then the program control to the RAM area and switches the power to the PROMs off via transistor switches to conserve power. It then starts monitoring the telecommand interface for possible boot instructions. This allows the configuration of the instrument in a flexible, but safe manner. If a START configuration is defined via TC the software continues accordingly. Otherwise the default START configuration inside the EEPROM is used. If this is corrupted, the original default configuration from PROM will be used.

A 512 kbyte radiation hardened EEPROM (Maxwell) contains additional program code and configuration information, which can be modified from the ground. 2 Mbyte mass memory RAM is used to store measurement data and buffer telemetry packets.

An Actel FPGA RT1280 implements the serial data transfer protocol to the IMA detector with an interface identical to the corresponding hardware used on the Rosetta mission. All interface lines are buffered via special circuits to protect the instrument from external noise effects.

The DPU board is controlled by a 24 MHz crystal which is divided down to 12 MHz and buffered inside an FPGA before it is used for FPGA and processor operations and also on the HK board. As the main FPGA needs 2.5 V operations voltage, this is generated by dedicated regulators directly on the DPU and on the HK board. The watchdog circuit inside the FPGA can be enabled by software. Then it has to be reset regularly by software access. Otherwise it issues a hardware reset to the whole DPU board after 16 s. Except for a special error message, the behaviour is identical to a boot sequence after power-up. The DPU board controls most detector voltages with direct access to the power supply board.

The HK board is controlled by a separate RT54SX32S FPGA, which maps all input and output functions into standard bus address space. It also implements the needed counters for detector pulses from the NPI and ELS.

Four eight-channel analog multiplexers select one out of 32 analog voltages to be monitored. They are digitalised by one 14-bit analog-to-digital-converter (ADC, LTC1419). Another 14-bit ADC monitors the ELS deflection voltage. Two 8-bit digital-to-analog-converters generate via 8 latching buffers the control voltages for NPD, NPI, ELS and the scanner.

The software is built around a real-time system with scheduler and interrupt handler. All executable routines are defined inside a routing table, which resides in EEPROM and can be modified during flight. In this way new or modified software routines can be stored inside a free area of the EEPROM, verified and added to the operating software by including their START address into this routing table. A macro feature of the telecommand handler offers the possibility to generate sequences of standard telecommands automatically according to a pre-defined list, reducing the need for complex telecommand groups to be up-linked over and over again. Besides sensor activation and parameter control, compression and averaging of measurement data allow the reduction of the amount of telemetry generated.

2.7. The scanner

The scanner platform was originally developed for the ASPERA-C experiment for the Russian Mars-96 project. Some modifications that were made for the Mars and Venus Express missions mostly concerned optimisation of the performance during long term operations and the reduction of its mass. The ASPERA-4 scanner serves also as a bearing structure for the ELS, NPI, and NPD sensors as well as the DPU and all electrical interfaces to the spacecraft.
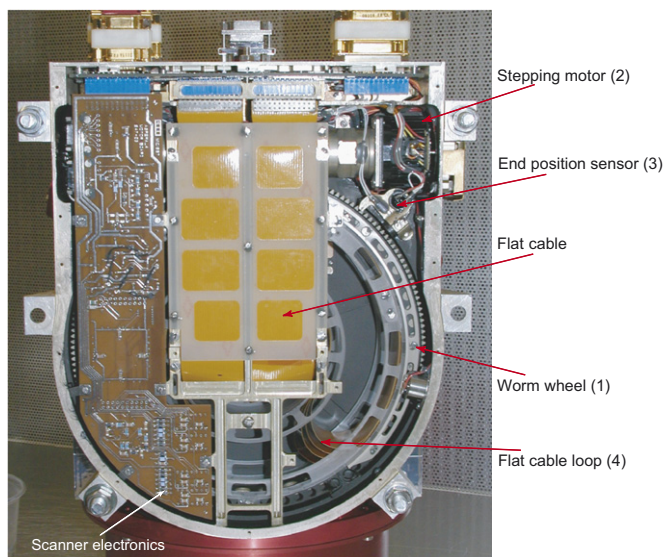
Fig. 30. ASPERA-4 scanner. Internal view. See explanations in the text.

Table 2
Technical data of the mechanical scanner platform

Parameter	Value	Unit
Maximum angle of rotation	±100	deg.
Angular movement per step, full step	0.0190	deg.
Angular movement per step, half step	0.0095	deg.
Angular position feedback resolution	0.05	deg.
Angular positioning accuracy	0.2	deg.
Operational rotation rate	1.5/3.0/6.0	deg./s
Maximum rotation rate	∼25.0	deg./s
Power dissipation	0.5–2.0	W
Platform load	3.7	kg
Maximum platform load	∼12	kg
Dimensions	$60 \times 254 \times 232$	mm^3
Mass	1.42	kg

Fig. 30 shows an internal view of the scanner. The large diameter worm wheel (1) to which the sensor assembly is fixed is rotated by a stepper motor (2) via a co-axial worm screw (not visible below the flat cable). The worm wheel is fixed to the structure with a large diameter angular contact ball bearing. During the scanner lifetime tests, several types of balls, including the ordinary already mounted in the original bearings, were tested. Finally a ceramic type (Si_3N_4) of balls was found to be the best suited for the use in bearing. The housing and the circular sensor platform were manufactured in a high-strength aluminium alloy. The technical data of the scanner is summarised in Table 2.

The motor driving electronics (not shown) is also located in the scanner and provides the motor control and driving. The position of the movable parts relative to the scanner is given by three magnetic sensors, two end-sensors at $0°$ and $180°$ (3), and one step counter. Due to the requirements on long-term operations no mechanical contact exists in the sensors. A feed-through cable loop (4) with six cables and six connectors, each cable with 26 conductors (a maximum of 156 connections possible) interfacing through D-SUB connectors provides the electrical interface of the whole instrument with the satellite electrical systems.

A worm gear type of mechanism was selected in order to provide self-locking without electrical power, to minimise friction and to obtain a high gear ratio. The platform is made as a plug-in unit towards the sensor assembly. Great efforts have been spent to reduce mass, volume, power consumption and out-gassing in vacuum as well as to achieve high reliability. On command the platform can be turned to an arbitrary position or perform continuous scanning at any rate of rotation up to the maximum.

The scanner also contains a locking mechanism to avoid possible movements of the platform during vibrations. The mechanism contains a wire which ties two small levers locking the worm screw axis. Applying by command a voltage to the wire burns it out and the levers are forced apart by a spring unlocking the axis.

2.8. Instrument accommodation

The instrument accommodation is shown in Fig. 31. While the IMA accommodation on Venus Express is the same as on Mars Express, the MU accommodation was changed to cope with the new thermal environment and respective changes in the instrument thermal design. The scanner spin axis, perpendicular to the instrument radiator, was co-aligned with the solar panel lateral axis, which under earth communication pointing is perpendicular to the ecliptic plane. This accommodation provides the shortest periods of the solar illumination of the radiator. The NPI and NPD sensors can be pointed in any direction within the solar panel hemisphere using the scanner. During continuous scanning the MCP biases of the NPI and NPD are automatically reduced at certain positions (commandable) when the Sun is within their field of view to avoid MCP saturation.

The IMA accommodation ensures the central plane of the field of view to be co-aligned with the ecliptic plane, when the spacecraft in Earth pointing mode. That provides the most effective coverage of the solar wind direction.

2.9. Instrument operations

The Venus Express orbit, polar with a pericenter between 250 and 400 km and an apocenter of 66 600 km, covers the region inside 3 Venus radii and does not extend in the distant tail. Fig. 32 shows several orbits through the mission in the cylindrical coordinates. The *x*-axis is the planet-Sun line and the *y*-axis the distance to the planet-Sun line. The modelled positions of the bow shock and ionopause are also shown taken from Biernat et al. (1999). The ASPERA-3 operation is thus organised in the way the in situ sensors, ELS and IMA, operate inside the bow show and 30 min before and after the inbound and outbound modelled bow shock crossing to monitor the upstream
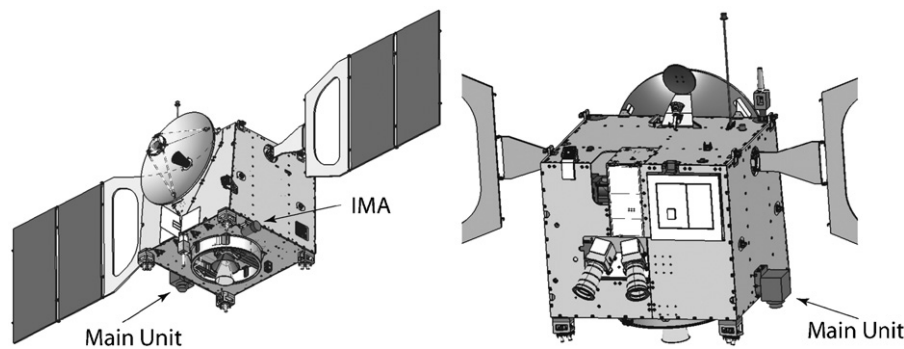
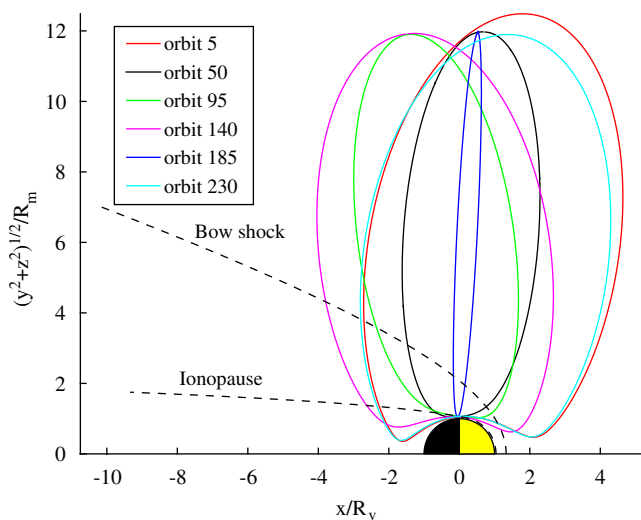Fig. 31. This figure shows where ASPERA-4 is located on Venus Express.

Fig. 32. Several Venus Express orbits in cylindrical coordinates. Modelled positions of the bow shock and ionopause are shown.

conditions. The periods of the ENA sensors, NPI and NPD, operations inside the bow shock are optimised to cover ENA fluxes originated in the ionosheath as well as backscattered ENAs and are calculated individually depending on the orbit configuration and the spacecraft pointing. Runs from distant vantage points outside the bow shock are also foreseen.

3. Conclusion

ASPERA-4 is a comprehensive plasma package that is intended to study the solar wind-Venus interaction. The primary goal is to quantitatively characterise non-thermal solar wind induced atmospheric escape. In combination with the MAG magnetometer on board (Zhang and et al., 2006), the Venus Express mission will also provide new insights in the field of space plasma physics. ASPERA-4 carries an electron spectrometer and ENA imagers to Venus for the first time. The ASPERA-4 ion spectrometer IMA is much more capable both in terms of mass resolution, energy coverage, and time resolution than the ion spectrometer that was flown previously on Pioneer Venus Orbiter. Finally, ASPERA-4 is a replica of the ASPERA-3 experiment orbiting Mars that provides a unique opportunity for the comparative magnetospheric studies.

References

Acuña, M.H., et al., 1998. Magnetic field and plasma observations at Mars: initial results of the Mars Global Surveyor mission. Science 279, 1676.

Alsop, C., Scott, S., Free, L., 1996. UV rejection design and performance of the PEACE electrostatic analysers. In: AGU Chapman Conference on Measurement Techniques in Space Plasmas, vol. 102, pp. 269–274.

Barabash, S., 1995. Satellite observations of the plasma-neutral coupling near Mars and the earth. IRF Scientific Report 228, Swedish Institute of Space Physics, Kiruna, Sweden, 1995.

Barabash, S., et al., 2007, The Analyzer of Space Plasmas and Energetic Atoms (ASPERA-3) for the Mars Express mission, Space Sci. Rev., doi:10.1007/s11214-006-9124-8.

Biernat, H.K., Erkaev, N.V., Farrugia, C.J., 1999. Aspects of MHD flow about Venus. J. Geophys. Res. 104, 12,617–12,626.

Biernat, H.K., Erkaev, N.V., Farrugia, C.J., 2000. MHD effects in the Venus magnetosheath. Adv. Space Res. 26, 1587–1591.

Biernat, H.K., Erkaev, N.V., Farrugia, C.J., 2001. MHD effects in the Venus magnetosheath including mass loading. Adv. Space Res. 28, 833–839.

Brace, L.H., Theis, R.F., Hoegy, W.R., 1982. Plasma clouds above the ionopause of Venus and their implications. Planetary and Space Sci. 30, 29–37.

Brecht, S.H., 1997. Solar wind proton deposition into the Martian atmosphere. J. Geophys. Res. 102, 11,287–11,294.

C:son Brandt, P., Barabash, S., Wilson, G.R., Roelof, E.C., Chase, C.J., 2000. Energetic neutral atom imaging at low (<10 keV) energies from Astrid: observations and simulations. J. Atmos. Solar Terrestrial Phys. 62, 901–910.

Cazaux, J., 1993. Some physical descriptions of the charging effects in insulators under irradiation. In: Baragiola, R. (Ed.), Ionization of Solids by Heavy Particles. Plenum Press, New York, pp. 325–350.

Deutscher, S.A., Borisov, A.G., Sidis, V., 1999. Formation of negative ions from fluorine projectiles scattered off a MgO(1 0 0) surface: theory. Phys. Rev. A 59 (6), 4446–4455.

Donahue, T.M., Hartle, E., 1992. Solar cycle variations in H^+ and D^+ densities in the Venus ionosphere: implications for escape. Geophys. Res. Lett. 12, 2449–2452.

Fok, M.-C., Moore, T.E., Collier, M.R., Tanaka, T., 2004. Neutral atom imaging of solar wind interaction with the Earth and Venus. J. Geophys. Res. 109 (A1), A01206.

Galli, A., Wurz, P., Lammer, H., Lichtenegger, H., Barabash, S., Lundin, R., Gregoriev, S., Holmström, M., Gunell, H., 2007. The hydrogen exospheric density profile measured with ASPERA-3/NPD. Space Sci. Rev., doi:10.1007/s11214-006-9089-7.

Gunell, H., Holmström, M., Barabash, S., Kallio, E., Janhunen, P., Nagy, A.F., Ma, Y., 2005a. Planetary ENA imaging: effects of different interaction models for Mars. Planetary and Space Sci. 54(2), 117–131.

Gunell, H., Holmström, M., Biernat, H.K., Erkaev, N.V., 2005b. Planetary ENA imaging: Venus and a comparison with Mars. Planetary and Space Sci. 53 (4), 433–441.

Hartle, R.E., Grebowsky, J.M., 1990. Upward ion flow in ionospheric holes on Venus. J. Geophys. Res. 95, 31–37.

Holmström, M., Barabash, S., Kallio, E., 2001. X-ray imaging of the solar wind–Mars interaction. Geophys. Res. Lett. 28 (7), 1287–1290.

Holmström, M., Barabash, S., Kallio, E., 2002. Energetic neutral atoms at Mars I: imaging of solar wind protons. J. Geophys. Res. 107 (A10), 1277.

Intriligator, D.S., Collard, H.R., Mihalov, J.D., Whitten, R.C., Wolfe, J.H., 1979. Electron observations and ion flows from the Pioneer Venus Orbiter plasma analyser experiment. Science 205, 116–119.

Intriligator, D.S., Wolfe, J.H., Mihalov, J.D., 1980. The Pioneer Venus Orbiter plasma analyser experiment. IEEE Trans. Geosci. Remote Sensing 18, 39–43.

Jans, S., 2000. Ionization of energetic neutral atoms for application in space instrumentation. Master's thesis, Philosophisch-naturwissenschaftlichen Fakultät, Universität Bern.

Johnstone, A.D., et al., 1997. PEACE: a plasma electron and current experiment. Space Sci. Rev. 79, 351–398.

Kallio, E., Barabash, S., 2000. On the elastic and inelastic collisions between precipitating energetic hydrogen atoms and Martian atmospheric neutrals. J. Geophys. Res. 105, 24,973–24,996.

Kallio, E., Luhmann, J.G., Barabash, S., 1997. Charge exchange near Mars: the solar wind absorption and energetic neutral atom production. J. Geophys. Res. 102, 22,183–22,197.

Krasnopolsky, V.A., Gladstone, G.R., 1996. Helium on Mars: EUVE and PHOBOS data and implications for Mars' evolution. J. Geophys. Res. 101 (A7), 15,765–15,772.

Luhmann, J.G., 1992. Comparative studies of the solar wind interaction with weakly magnetized planets. Adv. Space Res. 12 (9), 191–203.

Luhmann, J.G., Bauer, S.J., 1992. Solar wind effects on atmosphere evolution at Venus and Mars. In: Washington DC American Geophysical Union Geophysical Monograph Series, vol. 66, pp. 417–430.

Luhmann, J.G., Kozyra, J.U., 1991. Dayside pickup oxygen ion precipitation at Venus and Mars—spatial distributions, energy deposition and consequences. J. Geophys. Res. 96 (15), 5457–5467.

Marshall, F.J., Hardy, D.A., Huber, A., Pantazis, J., McGarity, J., Holeman, E., Winningham, J., 1986. Calibration system for electron detectors in the range from 10 eV to 50 keV. Rev. Sci. Instrum. 57 (2), 229–235.

McKay, C.P., Stoker, C.R., 1989. The early environment and its evolution on Mars: implications for life. Rev. Geophys. 27, 189.

Mihalov, J.D., Barnes, A., 1982. The distant interplanetary wake of Venus—plasma observations from Pioneer Venus. J. Geophys. Res. 87, 9045–9053.

Mihalov, J.D., Wolfe, J.H., Intriligator, D.S., 1980. Pioneer Venus plasma observations of the solar wind-Venus interaction. J. Geophys. Res. 85, 7613–7624.

Moore, K.R., McComas, D.J., Russell, C.T., Mihalov, J.D., 1990. A statistical study of ions and magnetic fields in the Venus magnetotail. J. Geophys. Res. 95, 12,005–12,018.

Moore, K.R., McComas, D.J., Russell, C.T., Stahara, S.S., Spreiter, J.R., 1991. Gasdynamic modeling of the Venus magnetotail. J. Geophys. Res. 96, 5667–5681.

Nagy, A.F., Cravens, T.E., Yee, J.-H., Stewart, A.I.F., 1981. Hot oxygen atoms in the upper atmosphere of Venus. Geophys. Res. Lett. 8, 629–632.

Norberg, O., Yamauchi, M., Lundin, R., Olsen, S., Borg, H., Barabash, S., Hirahara, M., Mukai, T., Hayakawa, H., 1998. The ion mass imager on the Planet-B spacecraft. Earth, Planets, and Space 50, 199–205.

Russell, C.T., Elphic, R.C., Slavin, J.A., 1980. Limits on the possible intrinsic magnetic field of Venus. J. Geophys. Res. 85, 8319–8332.

Schubert, G., Russell, C.T., Moore, W.B., 2000. Timing of the Martian dynamo. Nature 408, 666–667.

Stewart, A.I.F., 1980. Design and operation of the Pioneer Venus Orbiter ultraviolet spectrometer. IEEE Trans. Geosci. Remote Sensing 18, 65–70.

Zhang, T.L., et al., 2006. Magnetic field investigation of the Venus plasma environment: expected new results. Planetary and Space Sci. 53(13–44) 1336–1343.